NETWORK FLUX TRANSPORT: CONCEPT AND APPLICATION TO SOLAR MAGNETISM

by

Jon Thomas Eckberg

A thesis submitted in partial fulfillment
of the requirements for the degree

of

Master of Science

in

Physics

MONTANA STATE UNIVERSITY
Bozeman, Montana

November 2019

DEDICATION

I dedicate this thesis to my sons Jimmy and Charlie, for whom all my efforts are intended.

ACKNOWLEDGEMENTS

The original research described in this thesis was financially supported by subcontract 8100002707 from Lockheed Martin, in support of phases C/D/E of the NASA Interface Region Imaging Spectrograph (IRIS) mission, and supported by the continued encouragent of my advisor Prof. Charles Kankelborg.

VITA

Jon Eckberg was born in Havre, Montana in 1976. Jon graduated from Havre High School in 1995. Jon attended Montana State University - Bozeman from 1995 - 2001 and The University of Houston from 2002 - 2005 receiving a B.S. in Physics and a minor in Mathematics from the latter.

TABLE OF CONTENTS

TABLE OF CONTENTS – CONTINUED

LIST OF FIGURES

LIST OF FIGURES – CONTINUED

Figure Page

LIST OF FIGURES – CONTINUED

NOMENCLATURE

$\mathbf{B}$	Magnetic Field vector
B	Magnetic field magnitude
B_o	Polar mean magnetic field magnitude
Φ	Magnetic Flux
$\mathbf{v}$	Plasma velocity field
$\boldsymbol{\omega}$	Plasma vorticity field
ν	plasma viscosity
η	magnetic plasma diffusivity
σ_{IN}	STD of the instantaneous IN flux distribution
σ_{SG}	STD of the per-timestep IN flux contribution to the SG network
R_m	Magnetic Reynolds number $\equiv \frac{\mathbf{v} \cdot L}{\eta}$

ABSTRACT

We have developed a method to efficiently simulate the dynamics of the magnetic flux in the solar network. We call this method Network Flux Transport (NFT). Implemented using a Spherical Centroidal Voronoi Tessellation (SCVT) based network model, magnetic flux is advected by photospheric plasma velocity fields according to the geometry of the SCVT model. We test NFT by simulating the magnetism of the Solar poles. The poles of the sun above 55 deg latitude are free from flux emergence from active regions or ephemeral regions. As such, they are ideal targets for a simplified simulation that relies on the strengths of the NFT model. This simulation method reproduces the magnetic and spatial distributions for the solar poles over two full solar cycles.

INTRODUCTION

History

The sun plays a central role to all life on Earth, and to the Earth itself. It then comes as no surprise that humans have been observing the sun and attempting to understand its behavior as long as humans have recognized the Sun as a distinct feature in the sky. The first record of a manifestation of solar activity is believed to be from ancient China in the image of a black crow upon the red disk of the sun. A large active region seen with the naked eye while the sun is near the horizon may have inspired this symbolic image [Needham, 1959]. The first written mention of sunspots that survives to the current era comes from ancient Greece around 325 B.C.E. [Thomas and Weiss, 2008]. With the invention of the telescope in the early 1600's, Galileo Galilei as well as Johann Fabricius, Thomas Harriott and Christophe Scheiner began the direct study of the sun with optical magnification [Balogh and Thompson, 2009]. The era of telescopic observation of the sun began just in time to record the relative paucity of sunspots in the 17th and 18th centuries.

The nearly 11 year apparent periodicity of the solar cycle was first noticed by a German apothecary and amateur astronomer, Heinrich Schwabe in 1843. Schwabe was looking for periodic solar disk transits of a planet inside the orbit of Mercury. Apparently inspired by Schwabe's discovery, Englishman and amateur astronomer Richard Carrington began regularly observing the sun in 1853. Carrington eventually discovered that the latitude of sunspot appearances drifts towards the equator throughout the solar cycle. He also discovered the sun's differential rotation (DR) whereby it rotates faster at the equator than the poles, and determined the axial tilt of the sun with respect to the Earth's orbital plane. Carrington is also credited with the first observation and description of a visible light solar flare. His well documented observation of the sun on September 1st, 1859 of what is now called the Carrington event, along with his other solar observations, were eventually published by the Royal Society in 1863. Most of Carrington's discoveries were made independently around the same time by German Astronomer Gustav Spörer. The Spörer minimum is the name given to a period of fewer sunspots in the 16th century. Solar astronomy continued in this vein by documenting the visible manifestations of sunspots without connecting them to magnetism.

Regardless of Spörer's earlier work on the subject, E. W. Maunder receives much of the credit for historical research on sunspot records. [Maunder, 1904] This is based upon his early discovery and documentation of a now famous dip in the records of sunspot numbers. Named in 1976 [Eddy, 1976], The Maunder Minimum was an observed reduction in sunspot numbers from 1645 - 1715. Maunder also published the first study of the emergence of sunspots as a function of latitude and time. Plotting this relationship over 25 years demonstrated the first published butterfly diagram (Figure 1.1), though this term doesn't appear in the article [Maunder, 1904].

Based upon his observation of helical structures in the chromosphere above sunspots, George Hale began looking for magnetic fields in sunspots around 1908 [Hale, 1908]. Using the recently discovered Zeeman effect, Hale observed spectral line splitting consistent with the Zeeman effect in a magnetic field of 3 kilogauss. In the decade to follow, Hale discovered his polarity law [Thomas and Weiss, 2008]. Hale's law describes the strong statistical relationship between polarities of sunspot pairs and their orientation based on hemisphere.

While spectral line splitting was effective at determining sunspot field strengths, it was not sensitive enough to detect the fine structure of the sun's magnetic flux

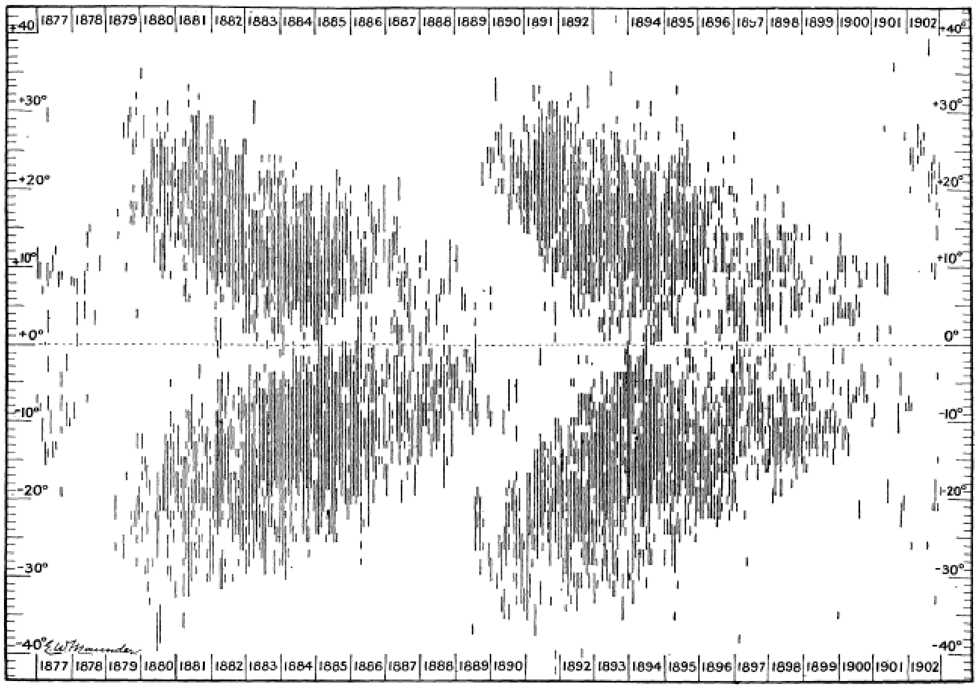

FIG. 8.—DISTRIBUTION OF SPOT-CENTRES IN LATITUDE, ROTATION BY ROTATION, 1877–1902.

Figure 1.1: The first butterfly diagram. Figure 8 from [Maunder, 1904].

distribution. In 1953 Babcock introduced the photoelectric magnetograph [Babcock, 1953]. Replacing manual methods, the photoelectric magnetograph used electro-optical components to automate the mapping of the solar magnetic field. The magnetograph used the longitudinal Zeeman effect in the spectral line of Fe I at 525.0 nm to create a map of rastered cross sections of the solar surface field. The technique had a reported noise level of 0.1 Gauss, and so could competently map the solar field to a field resolution of 10 Gauss [Babcock, 1959]. Using this technique on the 150 foot solar telescope at the Hale Solar laboratory, Babcock then discovered that the solar magnetic field reverses polarity every 11 years. Specifically, Babcock et. al. found that the field of the poles provides the majority of the magnetic flux for the solar magnetic dipole field. This resulted in the first evidence that the Hale's law cycle is connected to the behavior of the global field [Stenflo, 2017].

The concept of a macroscopic diffusion of magnetic flux occurring was first published by Leighton in 1964 [Leighton, 1964]. Observing that magnetic elements respond to surface convection similar to a random walk, Leighton calculated what he called the mixing coefficient. Using Leighton's length scale ($L = 1.5 \cdot 10^4 km$) and lifetime ($\tau = 7 \cdot 10^4 sec$) for a convection cell, we can calculate the effective value for macroscopic diffusivity D Using equation 1.1.

With the relation in equation 1.1, the diffusivity of particles subject to a random walk process in 2 dimensions is $\approx 803 \frac{km^2}{sec}$.

$$D = \frac{L^2}{4\tau} \tag{1.1}$$

To conclude this survey of relevant solar astronomy history for this thesis, we discuss the discovery of the solar chromospheric network. The solar chromospheric network is the qualitatively net-like structure that appears as an intensity enhancement when the sun is imaged in chromospheric spectral lines. Specifically, the spectral lines of Hydrogen-α (red) and Calcium II-K (ultraviolet) are typically used as the diagnostic lines for this phenomenon [Malherbe and Dalmasse, 2019]. It was published in 1964 that the velocity fields measured by Simon and Leighton were highly correlated with the fine structure of the magnetic fields on the solar surface [Simon and Leighton, 1964]. Described as having a cellular geometry, the cells of diverging velocity fields were observed to reside between the network lanes (see Figure 1.2 for example).

Background

We transition to discussing the relevant solar physics as it is currently understood with modern techniques and findings. The development and understanding of the

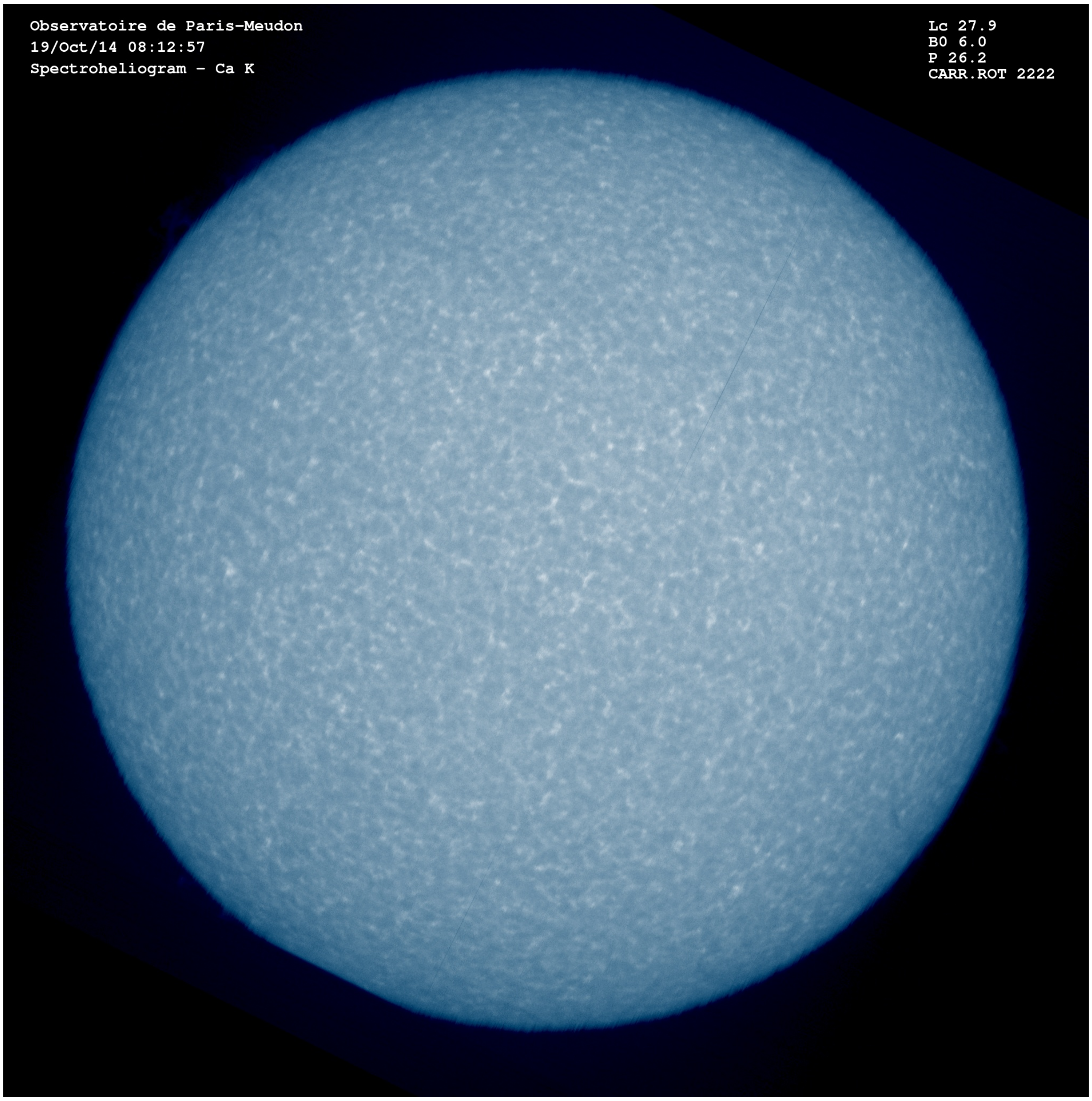

Figure 1.2: Ca II K image of the sun from the Paris Observatory's Meudon Spectroheliograph. Image shows the network of bright network lanes between darker cellular structures.

science of fluid dynamics and planetary physics led to the simulation of the Earth's atmosphere as an entire system. Similarly, modern solar physics is actively engaged in simulating the dynamics of the sun as a star, as well as inferring processes that are not directly observable. This involves simulation of physical processes from the core of the star to the physics of the Corona and solar wind. By comparison, the scope of this thesis is very narrow. The concepts here within, primarily involve the solar photosphere and the processes operating in the observable near surface. We now begin description and discussion of the relevant near surface physics with the remainder of this section.

Solar Magnetism

Convective stars are intrinsically magnetic objects. Because plasma is electrically conductive, convective sun-like stars convert kinetic energy into a magnetic field energy throughout its lifetime via the dynamo effect [Rincon, 2019]. This magnetic field persists throughout the convective life of the star. Conversion and modification of magnetic flux modulates the spin rate and global fluid flows over the lifetime of the star. For a star with a convective envelope like the Sun, magnetic flux is produced and transported through the convective zone to emerge from the solar surface. As these fields protrude from the photosphere, they become the magnetic field of the solar atmosphere known as the corona. As these emerged fields are modified and reconnected by surface flows and coronal interactions, they result in the production of energetic phenomena such as solar flares, Coronal Mass Ejections (CME) and the modulation of the Galactic Cosmic Ray (GCR) flux observed within the Heliopause.

Bundles of magnetic flux are constantly emerging to the solar atmosphere, modulated by the ≈ 22 year solar cycle. The convective flows on the surface are constantly modifying these regions of magnetized plasma, both by joining adjacent flux regions, and by splitting them. The largest regions of coherent, kilogauss magnetic flux are commonly referred to as sunspots. Sunspots emerge from the solar surface in pairs of opposite polarity magnetic flux in the range of $10^{20} - 10^{22}$ Maxwells of flux [Schrijver and Zwaan, 2000, Thomas and Weiss, 2008]. They represent a helically twisted, cylindrical region of magnetic flux, referred to as a flux rope or flux tube. This flux emerges from, and intersects with the photosphere in two regions which have radial or anti-radial fields. To quantify the magnetic flux in the solar atmosphere, we count the flux as it intersects the photospheric surface. Mapping the flux distribution on the visible solar surface is accomplished by taking a magnetogram.

Sunspots become visible or emerge from the sun with a frequency dependent upon latitude and phase of the approximately 11 year solar cycle. After emergence, the sunspot slowly decays and shrinks as the surface convection turbulently shreds the sunspot and transfers the flux into the adjacent network. Network flux is lost by apparent cancellation of opposite polarity regions. The disappearing surface flux undergoes a dynamic combination of field cancellation, re-connection and, subduction in the network downflows [Harvey et al., 1999, Iida et al., 2010].

Flux is also advectively diffused over the solar surface. Sunspot pairs and their surrounding area are referred to as Active Regions (AR) as they appear bright and dynamic in the coronal wavelengths of extreme ultraviolet (EUV) and soft X-ray (SXR). Sunspots produce their characteristic dark spot regions of the photosphere in visible wavelengths of light. The flux transferred to the local network from AR increases the brightness of the surrounding regions in visible and near UV. The bright network is called faculae if observing the photosphere, or plage if observing the chromosphere.

Another source of new magnetic flux that emerges from the photosphere is the Ephemeral active Region (ER). These are flux tubes with much less flux than a sunspot, in the range of $10^{18} - 10^{20}$ Maxwells of flux. [Schrijver and Zwaan, 2000, Thomas and Weiss, 2008] These usually emerge inside supergranule convection cells and are much less apparent in visible wavelengths. ER do not have the amount of flux necessary to darken the visible photosphere, so are more detectable with a magnetogram or as EUV/SXR bright points.

The primary process which defines the solar cycle is magnetic flux emerging to the surface in activity bands. These bands begin as flux emergences near 55° latitude and migrate towards the equator [McIntosh et al., 2014, Srivastava et al., 2018]. The flux emerged from the activity bands initially increase in size and number as they descend towards the equator. At an average mid-latitude they peak in flux then begin diminishing in strength and effectively terminate with the mirroring activity band across the equator in the opposite hemisphere [Petrie, 2017]. The so called butterfly diagram which describes the emergence of sunspots throughout the solar cycle, constitutes the most intense portion of an activity band's life-cycle. It is the nearly 11 year period of time between the activity of these bands that has been considered the determinative period of a solar cycle. The solar cycle was originally observed in the sunspot number, with the period defined by approximately 11 years between maxima. The Hale's law polarity of successive activity bands reverses every 11 years so to complete a full solar cycle period takes 22 years.

To better understand the nature of the solar photosphere for our purposes, lets look at some relevant dimensionless quantities which will tell us about the medium we are simulating. The magnetic Reynold's number (R_M) is the ratio of the product of the characteristic velocity and length scale of a system $U \cdot L$, to the magnetic diffusivity (η). For the photosphere of the sun, (R_M) $>>$ 1 meaning flux is advected with the plasma flow and microscopic magnetic diffusion is unimportant.

Also, the magnetic Prandtl number (Pr_m) at the solar photosphere is $\approx 10^{-5}$, meaning the parameter describing plasma viscosity (ν) is much smaller than the parameter describing magnetic diffusivity (η). This might mean that resistive diffusion of magnetic flux in the solar photosphere is significant. However, resistive diffusion is not observed at the length and time scales applicable to the solar surface.

As such, we can consider magnetic flux as existing in discrete flux elements (FE) without a loss of flux due to Ohmic decay.

Differential Rotation

The spatial distribution of magnetic flux in the photosphere is modified by global scale plasma flows, the solar equivalent of the prevailing winds as found on Earth. The convection zone of the sun as a fluid shell is rotating, and also differentially rotating as the angular velocity of the surface flows is larger at lower latitudes. This differential rotation (DR) is a common occurrence for most stellar bodies and many gaseous planets [Tassoul, 2000].

Meridional Flow

Another global scale flow of stellar material is the Meridional Flow (MF). Although it is a relatively slow flow compared to surface convection, the MF has been detected by both observing magnetic features [Komm et al., 1993] and by helioseismology [Giles et al., 1997]. The velocity field of the MF advects surface plasma and magnetic regions from the equator to the poles and forms effectively two convergent convective cells, one for each hemisphere [Tassoul, 2000]. Figure 1.3 from [Hathaway and Upton, 2014] is a map of the latitudinal mean MF as tracked from 1996 to 2013 and demonstrates the consistent poleward flow and the fluctuating amplitude of the MF.

Despite a smaller speed, MF plays a larger role than DR in determining the surface distribution of magnetic flux on the sun. Because AR and ER do not emerge at latitudes above 55°, MF determines the concentration of uni-polar flux at the solar poles during solar cycle minimum. This is because the MF has a source-sink geometry and drives polar accumulation of flux. DR has a circulating geometry about the poles with no accumulative result.

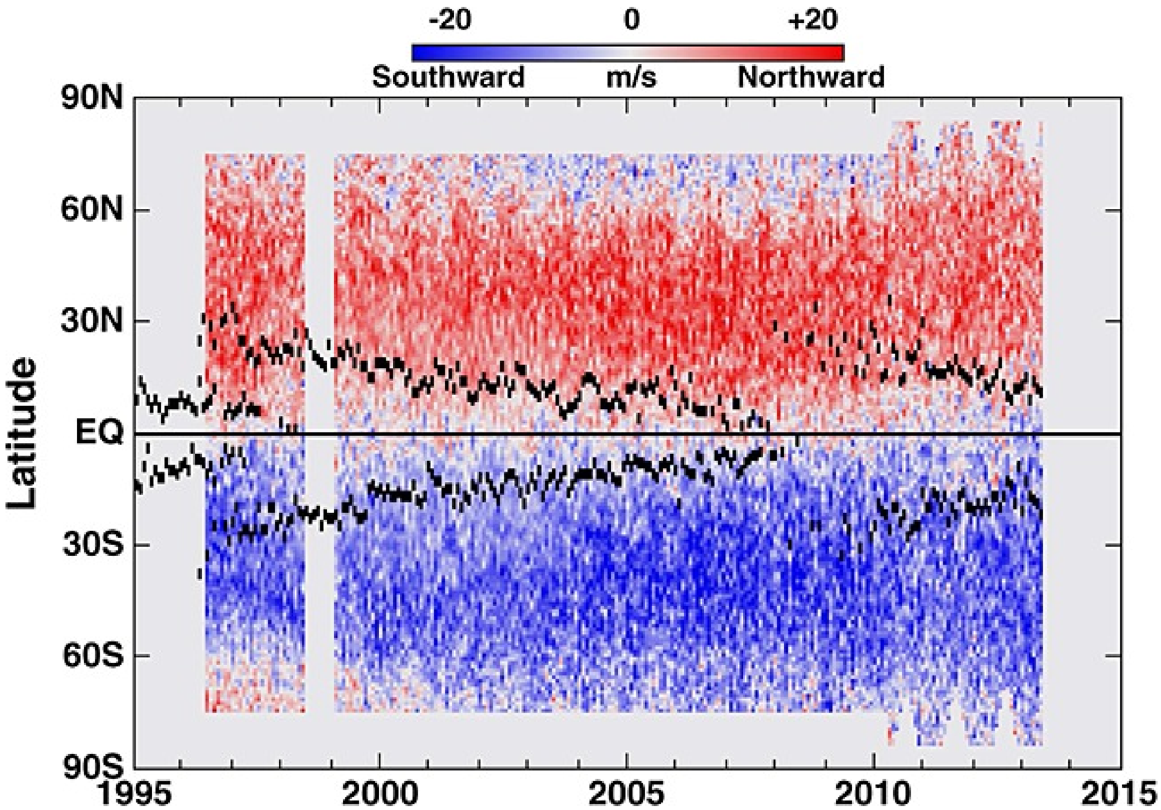

Figure 1.3: Figure 5 from [Hathaway and Upton, 2014]. MF profile obtained by feature tracking from HMI and MDI magnetograms from May 1996 to July 2013.

Surface Convection

Magnetic flux is also modified by two smaller scales of local surface flows, the granulation and supergranulation near surface convection cells. The displacement of surface magnetic flux in the convective velocity fields results in a locally correlated transport of magnetic flux [Giannattasio et al., 2019] similar to a random walk process. Granulation and Supergranulation (SG) are the surface convection processes currently most observable on the solar surface [Nordlund et al., 2009]. The visible manifestation of granulation was first described by William Herschel in 1801 [Herschel, 1801] as he described the surface of the sun as appearing mottled or granular.

SG convection cells are the primary source of the consistent horizontal velocity fields to transport emerged flux to the SG network. Rincon et. al demonstrated the relative stability of the SG network over a 24 hour time period [Rincon and Rieutord, 2018]. A map of the Finite Time Lyapunov Exponent (FTLE) of the solar surface velocity field shows a distinct, coherent network over this time scale. SG is responsible for determining the spatial distribution of flux emergence by transporting magnetic flux pairs to the surface with convection. The SG network, which forms at the boundary between SG cells, collects magnetic flux and recycles it back into the SG convection process through the collection, concentration, and subduction of surface flux. The distribution of SG cell areas has been observed and described using various methods [Hagenaar et al., 1997]. Inside the cells of the SG network is a domain called the Intra-Network (IN). This is the region where flux resides between granules in the granulation network. This IN flux is then carried into the network.

Because of the multi scale surface convection, the solar surface presents a turbulent landscape of plasma fluids convecting, diverging and colliding. The equilibrium behavior of magneto-hydrodynamic (MHD) turbulence evolves to a configuration where vorticity becomes concentrated in thin tubes or filaments. The magnetic field in the MHD formulation can be shown to behave similarly [Biskamp, 2003]. This behavior can be explained by noting the similarity of the MHD equations 1.2 and 1.3, for the vorticity and magnetic field when Lorentz forces can be ignored [Biskamp, 2003]. This condition requires a sufficiently weak field and is not present in regions of strong magnetic field, such as in a sunspot umbra or near a large network vertex flux concentration. However, for most of the photosphere this condition is valid. And even where the magnetic field is too intense and Lorentz forces can not be ignored, the locations of strong vorticity and magnetic field will still be highly spatially correlated. This correlation is also observed in MHD simulations of the photosphere. Rempel notes that larger and longer lived flow structures are necessary

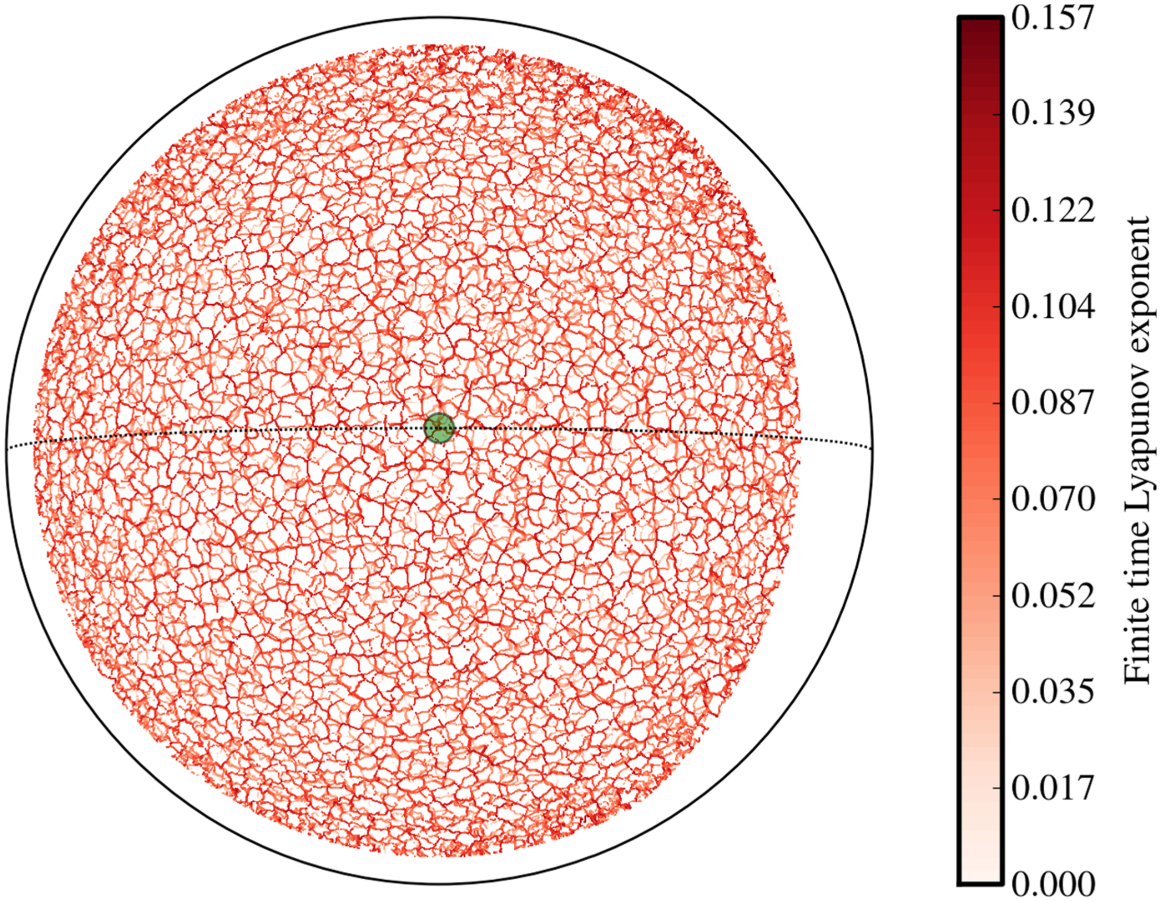

Figure 1.4: A map of the FTLE of solar surface horizontal flows over 24 hours using SDO data (October 8, 2010). The green circle is 15 Mm in radius. Figure 18 from [Rincon and Rieutord, 2018].

for kiloGauss density concentrations of magnetic flux [Rempel, 2014].

The magnetic Prandtl number (Pr_m) is the parameter describing the ratio of plasma viscosity (ν) and magnetic diffusivity (η). At the solar photosphere it is $\approx 10^{-5}$, meaning that magnetic dissipation is stronger than kinematic dissipation. If $(Pr_m) = 1$, equations 1.2 and 1.3 would have exactly the same solutions. Qualitatively we can say that downflows with a radially aligned vorticity, will accumulate radially aligned magnetic fields. In effect because of surface convection, the photosphere self segregates into unmagnetized plasma and a filamentary magnetized plasma. The surface geometry of the convective cells produce divergent flow fields which meet the flow fields of adjacent convection cells and form the network. The center of the divergent flow is where the volume of the upward flowing convection occurs. The network is then where the down flow occurs, between cells. Between SG, in the network where magnetic flux accumulates, photospheric plasma vortices have been observed and documented at network vertices [Langfellner et al., 2015, Requerey et al., 2018]. These are the plasma downflow portions of the SG convection cycle.

$$\frac{\partial \boldsymbol{\omega}}{\partial t} + \mathbf{v} \cdot \nabla \boldsymbol{\omega} = \boldsymbol{\omega} \cdot \nabla \boldsymbol{v} - \boldsymbol{\omega} \nabla \cdot \mathbf{v} + \nu \nabla^2 \boldsymbol{\omega} \tag{1.2}$$

$$\frac{\partial \mathbf{B}}{\partial t} + \mathbf{v} \cdot \nabla \mathbf{B} = \mathbf{B} \cdot \nabla \mathbf{v} - \mathbf{B} \nabla \cdot \mathbf{v} + \eta \nabla^2 \mathbf{B} \tag{1.3}$$

Polar Field

At latitudes poleward of ±55°, emergence of large elements of magnetic flux doesn't appear to occur in any significant quantity [Petrie, 2017]. Polar magnetic flux appears to originate only in AR or ER between ±55° latitude and is carried to the polar caps by the MF [Harvey, 1993, McIntosh et al., 2014]. As a result, the change in net flux in the polar regions is primarily due to surface advective transport conducting regional flux imbalances towards the poles.

The Sun's polar magnetic field has been identified as a reliable proxy for the current phase of the solar cycle [Muñoz-Jaramillo et al., 2013, Priyal et al., 2014, Petrie, 2015]. This behavior had also been studied with non-solar parameters to understand the magnetic cycles of Sun-like stars [Schrijver and Title, 2001]. Over the course of a solar cycle, the solar poles transition from a maximum of net signed flux, through quasi-neutrality to a maximum of the opposite sign of magnetic flux. This "polar cycle" advances in nearly anti-phase with the solar cycle and with the same

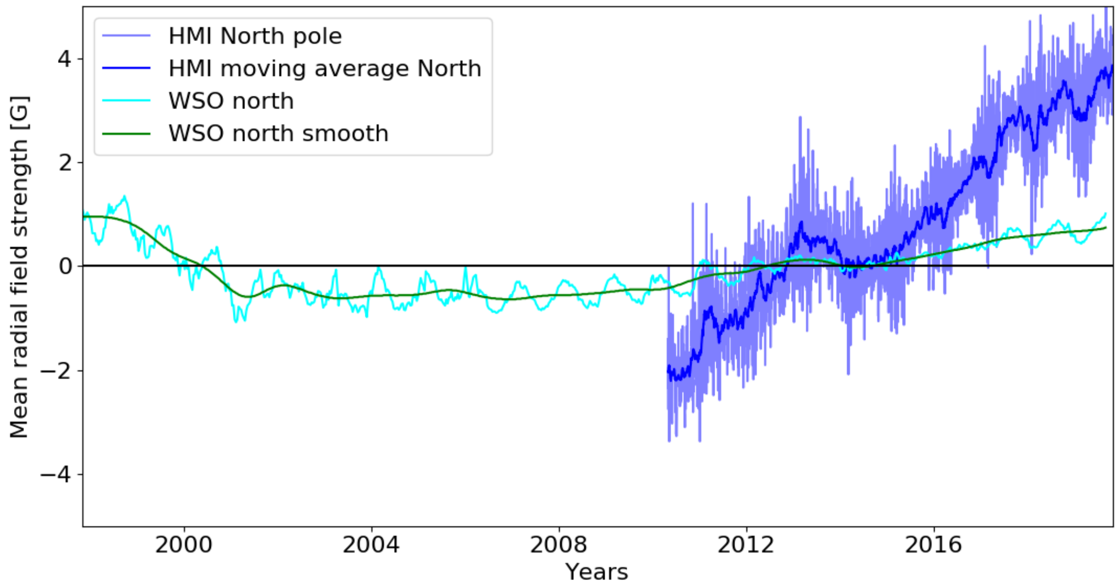

Figure 1.5: Plot of WSO [Svalgaard et al., 1978] and HMI [Sun et al., 2015] observed mean polar field.

periodicity. The poles transition polarities through neutrality gradually and remain near a maximal flux imbalance for about half of the cycle. Transitions are bursty and not always monotonic as they are responding to the orientation, strength, and decay rates of emerged AR.

The average magnetic field in the sun's polar regions is typically 2-4 Gauss during polar maximum average field, usually coincident with solar minimum. Figures 1.5 and 1.6 show the average polar magnetic fields from the last two decades as observed by the Wilcox solar observatory (WSO) [Svalgaard et al., 1978] and The Helioseismic and Magnetic Imager (HMI) [Scherrer et al., 2012]. The HMI result is an integration of the entire observable polar field poleward of $\pm 60°$ [Sun et al., 2015]. WSO observes a much smaller portion of the high latitude poles, and reports a typically smaller magnitude for the polar field. Despite this, the two techniques are in qualitative agreement.

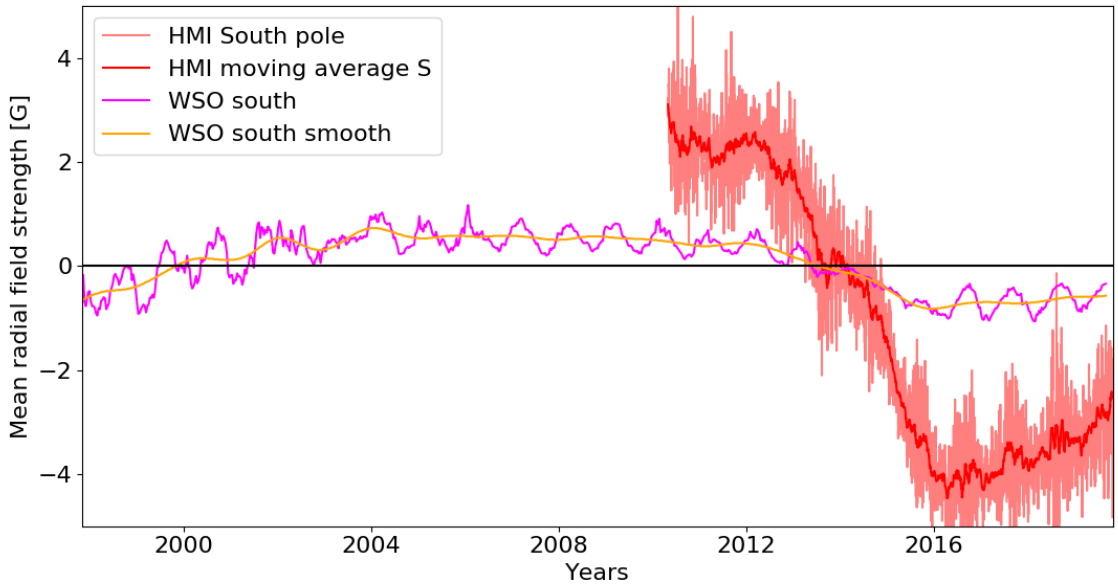

Figure 1.6: Plot of WSO [Svalgaard et al., 1978] and HMI [Sun et al., 2015] observed mean polar field.

During periods of high polar field, visible spectrum features of magnetic flux concentrations are present. These features are called faculae and are also found near AR at lower latitudes. They are regions of high magnetic flux appearing stochastically due to photospheric velocity fields. Polar faculae numbers are used as a consistent proxy for polar magnetic field [Sheeley, 1964]. Observations made during the polar maximum field in 2005 indicate that about 1/4th of the polar faculae flux is contained in the minority polarity [Blanco Rodríguez et al., 2007].

Polar Flux Distribution

Observations by the Solar Optical Telescope (SOT) of the (ISAS/JAXA) satellite Hinode [Tsuneta et al., 2008] have described the polar flux quantity and distribution over much of a solar cycle in unprecedented detail [Shiota et al., 2012]. The binned distribution function of polar flux element magnitudes were calculated and plotted

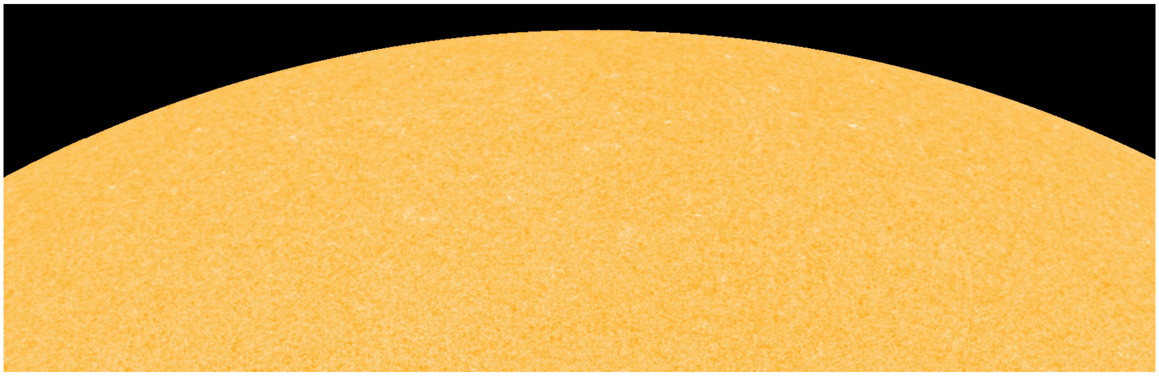

Figure 1.7: Image of faculae near the north solar pole taken by HMI on 10/24/2019. Faculae are the bright regions in the relatively dark photosphere.

(see figure 1.8: top row). The binned polar area covered as a function of magnetic flux was also calculated and plotted (see figure 1.8: bottom row). During polar maximum, the distribution of binned polar area peaks at around 10^{19} Maxwells (Mx) for the dominant polarity and at 10^{16} Mx for the non-dominant polarity. During and near polar minimum, both polarities peak near 10^{16} Mx as the poles are magnetically neutral. This minimal value represents a quiet sun distribution as seen at the high obliquity of the poles. A similar distribution was also observed for a quiet sun region near disk center demonstrating that observational constraints weren't a limiting factor in this analysis. No comprehensive model has yet been proposed to account for these essential characteristics of the polar flux distribution. Although it may be tempting to infer a power-law behavior from the heavy-tailed behavior of the binned distributions in Shiota et. al., extra care must be taken in fitting continuous, analytical distribution functions to binned data [Virkar and Clauset, 2014].

The magnetic flux distribution has a strong dependence upon the method of observation and interpretation of the data. Differing methods of counting and clustering flux into coherent elements can result in very different distributions from the same underlying magnetogram data set. Because magnetic field measurements

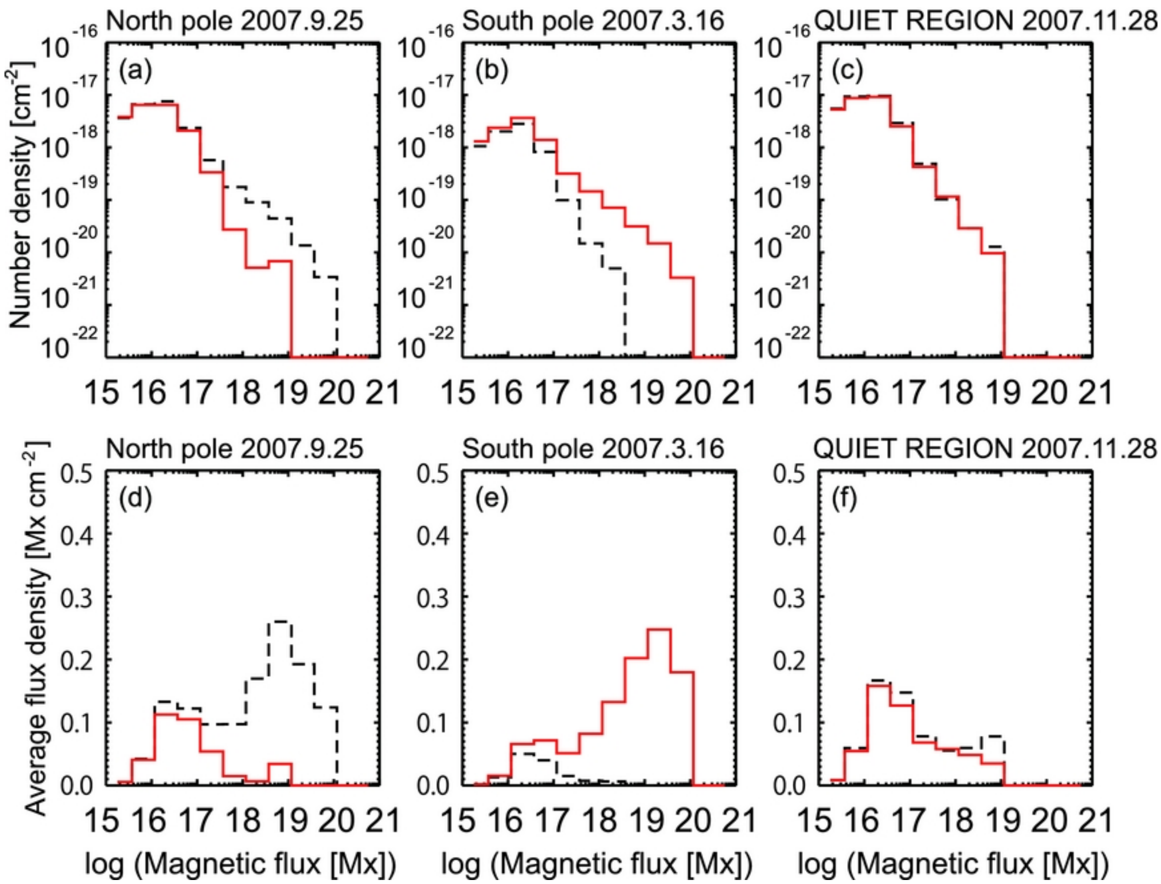

Figure 1.8: Figure 2 from [Shiota et al., 2012] showing snapshots of polar flux distributions from different poles at different solar cycle phases.

are made using the Zeeman effect, the measured quantity is the mean of the signed flux density in each magnetogram pixel, resulting in a measurement that is resolution sensitive. The concept of a magnetic feature has even come under criticism due to some of the unphysical assumptions contained therein [Gorobets et al., 2017].

The Hanle effect is a quantum process that affects polarization coherence in certain elemental emission lines found in the photosphere [Stenflo, 1982]. The unsigned flux density can be determined using the Hanle effect and through simulation [Borrero et al., 2017]. While the unsigned magnetic flux density is known to be larger in the core of granules, the incoherent and non-uniform direction of these fields make these unobservable using conventional magnetograms.

As a result, when we discuss flux distributions in this thesis, we are referring to coherent and mostly radially oriented magnetic fields confined to the solar network and smaller scale granule network. Consequently, we may anticipate that increasing spatial resolution and sensitivity will continue to reveal smaller and smaller elements of balanced magnetic flux [Solanki et al., 2010] as the magnetic polarization of regions results in larger flux elements accumulating the majority of the imbalance. The upcoming DKIST observatory should confirm this behavior as it will decrease the scale of resolvable magnetic features to a theoretical minimum [Martinez Pillet et al., 2019]. The ultimate aim of this paper is to introduce the network flux transport (NFT) model, using polar observations and analysis of Shiota et. al. [Shiota et al., 2012] as a guide. To date the best observational analysis of the polar magnetic flux distribution is that of Shiota et. al. Figure 1.8 shows 3 examples of observed flux distributions in the north and south polar regions and near disk center. Also shown are the distributions of the quantity of area covered by flux clusters binned by the total flux of the cluster.

Because the poles of the sun form two sinks for magnetic flux due to the convergent polar flow from the MF, They polarize in a large scale manner that isn't possible at lower latitudes except in the vicinity of an active region evolving into a region of plage. Consequently, the poles of the sun are usually magnetically polarized as they are occupied by flux of mostly one magnetic polarity. A polarized flux distribution behaves differently than those near the equator except possibly for small, local regions near an AR or ER emergence. The quiet sun solar flux magnitude distribution at lower latitudes should not be treated as valid near the poles [Parnell et al., 2009, Muñoz-Jaramillo et al., 2015].

Surface Flux Transport models

If the goal is to model the magnetic behavior of the solar surface and atmosphere, this can be accomplished by using SFT. This is done by simulating the distribution and dynamics of the magnetic flux at the photosphere and using that solution as a boundary condition for the dynamical evolution of the chromosphere and corona. To accomplish this, we can use the concept of a Surface Flux Transport model.

The magnetic Reynold's number (R_M) is the ratio of the product of the characteristic velocity and length scale of a system to the magnetic diffusivity: $\frac{U \cdot L}{\eta}$. For the photosphere of the sun, $R_M \gg 1$. This results in magnetic flux being advected with the plasma flow. Microscopic magnetic diffusion is relatively unimportant. This results in magnetic flux existing in a "frozen in" condition, and moving only with the plasma [van Ballegooijen et al., 1998].

$$\frac{\partial \mathbf{B}}{\partial t} = \boldsymbol{\nabla} \times (\mathbf{v} \times \mathbf{B}) + \eta \nabla^2 \mathbf{B} \tag{1.4}$$

In MagnetoHydroDynamics (MHD), the evolution of the magnetic field can be represented by the magnetic convection-diffusion equation as in equation 1.4. A solution to the magnetic MHD equation in spherical geometry and using the global scale flow fields of the sun should reproduce observations of solar magnetic flux. Because $R_M \gg 1$, we say that the flux is frozen in to the plasma and we can ignore the second diffusive term in equation 1.4 due to microscopic magnetic diffusion in equation 1.4 [van Ballegooijen et al., 1998]. The surface of the sun though, is an extremely dynamic domain for magnetic flux and exhibits complicated transport properties [Giannattasio et al., 2019]. One method of finding solutions to the ADP in spherical coordinates is by using Spherical Harmonics (SH) to represent the solution for $\mathbf{B}$. The velocity fields would be due to DR and MF and surface convection is represented by the diffusion term with an empirically derived macroscopic diffusivity η [Wang, 2017]. This is similar to the microscopic magnetic diffusion in the equation 1.4, but represents an empirical macroscopic diffusion due to unresolved convective turbulence.

In practice, a finite series of SH eigenfunctions are used to approximately reproduce the solution of equation 1.4, the magnetic Advection-Diffusion PDE (ADP) equation. For solutions with sharp, small wavelength features, a computationally impractical number of SH eigenfunctions could be required. Solution to the spatial magnetic flux distribution cannot be well represented by SH solutions of the ADP equation 1.4.

For representing the acoustic mode oscillations of the sun, SH are entirely appropriate as these are the eigenfunctions of the Laplacian differential operator in spherical coordinates [Basu, 2016]. Representing the network geometry of the solar magnetic distribution with spherical harmonic wavefunctions is less than optimal. Our flux free magnetic evolution equation (eq. 1.4) does not contain a Laplacian in the flux-free form. While it is possible to represent any scalar function on the surface of a sphere with an infinite series of SH, the convergence of this representation for a complicated function will take a large number of terms and is subject to numerical artifacts such as the Gibbs overshoot.

Also, the diffusivity that has been required to reproduce the observed flux distribution on the solar surface is can be at least twice that of the observed SG diffusivity. Whitbread et al. found optimal values of $\approx 350 - 500\frac{km^2}{sec}$ were needed for the applied diffusivity. This issue is avoided by Upton et. al. with the use of explicit velocity fields to reproduce the advection due to SG. This method though results in numerical instabilities which are then attenuated by adding an artificial diffusion term to the PDE to promote numerical stability [Upton and Hathaway, 2014].

For a review of the SFT concept, Jiang et. al. gives a comprehensive version and Wang et. al. looks at the application of SFT to simulating the cycle of changing polar fields [Jiang et al., 2015, Wang, 2017]. Some degree of parameter tuning must always occur to ensure the simulation output approximates physical observations [Whitbread et al., 2017]. One way to minimize the number of these decisions that must be made for the simulation to approach physical behavior would be to represent the physical variables with an appropriate geometry. The advent of the Advective Flux Transport (AFT) model was made to incorporate observed synoptic solar data [Upton and Hathaway, 2018], to prevent the simulation from departing too far from observation.

Motivation

Ultimately, we wish to represent the distribution of magnetic flux on the solar surface without restricting the description to canonical techniques such as PDEs and SHs. These techniques are successful for more fundamental physics, but may be less appropriate for a complex system with dynamically determined emergent behavior like the sun. To try another approach, we can represent the solution to the spatial distribution of magnetic flux in its natural geometry. Because SG continuously confines most coherent flux to the network, we can represent magnetic flux as scalar values of network elements.

Summary

In the following sections of this thesis, we will attempt to do the following:

1. Section: NFT
   (a) Describe the Network Flux Transport (NFT) concept.
   (b) Describe the conceptual methodology for performing the NFT simulation.
   (c) Identify some problems for which the NFT concept is suited to simulate in the limited setting of a masters thesis.
2. Section: Results
   (a) Simulate effective Supergranular diffusivity and discuss applicability.
   (b) Simulate the polar field of the sun through several solar cycles and compare to observations.
   (c) Simulate and track the magnetic flux distribution of the sun and compare to observations.
3. Section: Conclusion
   (a) Summarize results from previous section.
   (b) Discuss the validity and limitations of NFT approach.
   (c) Identify further questions to be answered by means of an NFT simulation.

NETWORK FLUX TRANSPORT

Concept

Network Flux Transport (NFT) is the name we give to the following simulation method for a surface flux transport in the presence of surface convection cells, such as SG. NFT is best described as a Finite Element Method with sources on a new random Voronoi tesselation for every timestep. In a conventional FEM discretization, the simulated elements are the faces of the mesh while the edges and vertices of the mesh provide boundary conditions and source regions [Gockenbach, 2006]. For NFT however, this relationship is reversed. The simulated elements are the edges and vertices, while the faces of the mesh provide boundary conditions and source regions. While we apply NFT to simulating the sun in this thesis, the NFT concept could be applied to other stars or phenomena. The key aspects of the NFT are listed below:

1. The network has a Voronoi geometry.
2. The network Voronoi cells have a stationary distribution of areas and length scales.
3. Flux accumulates at the vertices of the Voronoi network.
4. The vertex flux value is the scalar sum of all flux entering the vertex network. This is the merging process for NFT.
5. The Voronoi cellular network is memory-less. It has a new configuration after one average timescale of the network cell.
6. The magnetic flux is essentially the memory of the system, possessing both a quantity of magnetic flux, and a position.

7. The initial network flux is advected and fragmented by a divergent flow field within the network cell of the new network.

8. The network vertices and magnetic flux are advected by the global scale velocity fields of DR and MF.

9. A net neutral quantity of positive and negative magnetic flux emerges from a network cell and enters the surrounding network in normally distributed quantities.

Once these relatively simple concepts are implemented in a numerical simulation, much of the complex dynamics of the solar magnetic flux can be reproduced. We now discuss and justify the above aspects of NFT that we assume to simplify the physics.

The application of the Voronoi tessellation [Voronoi, 1908] to the geometry of the solar photosphere and atmosphere is not new. In NFT, we use the polygonal Voronoi cells to represent the convection cells. The network between cells is represented by the Voronoi vertices and edges. Flux moves in response to the global scale velocity fields, and is advected to the nearest vertices after each timestep. NFT utilizes the approximation that flux on the surface can be treated as discrete quantities confined to the network. The flux occupies a region of the network contained within the Delaunay dual of a vertex. It is essentially a "Y" shaped region of the network. These regions are small with respect to the desired spatial scale of the simulation and can be treated as having a negligible network width. The network topology is constantly changing due to the initiation and exhaustion of the convection cells. Hagenaar et al. describes a similar concept to NFT involving flux moving within the network around a SG for conceptual purposes and to justify the step-length in their simulation [Hagenaar et al., 1999](pp. 940, last paragraph).

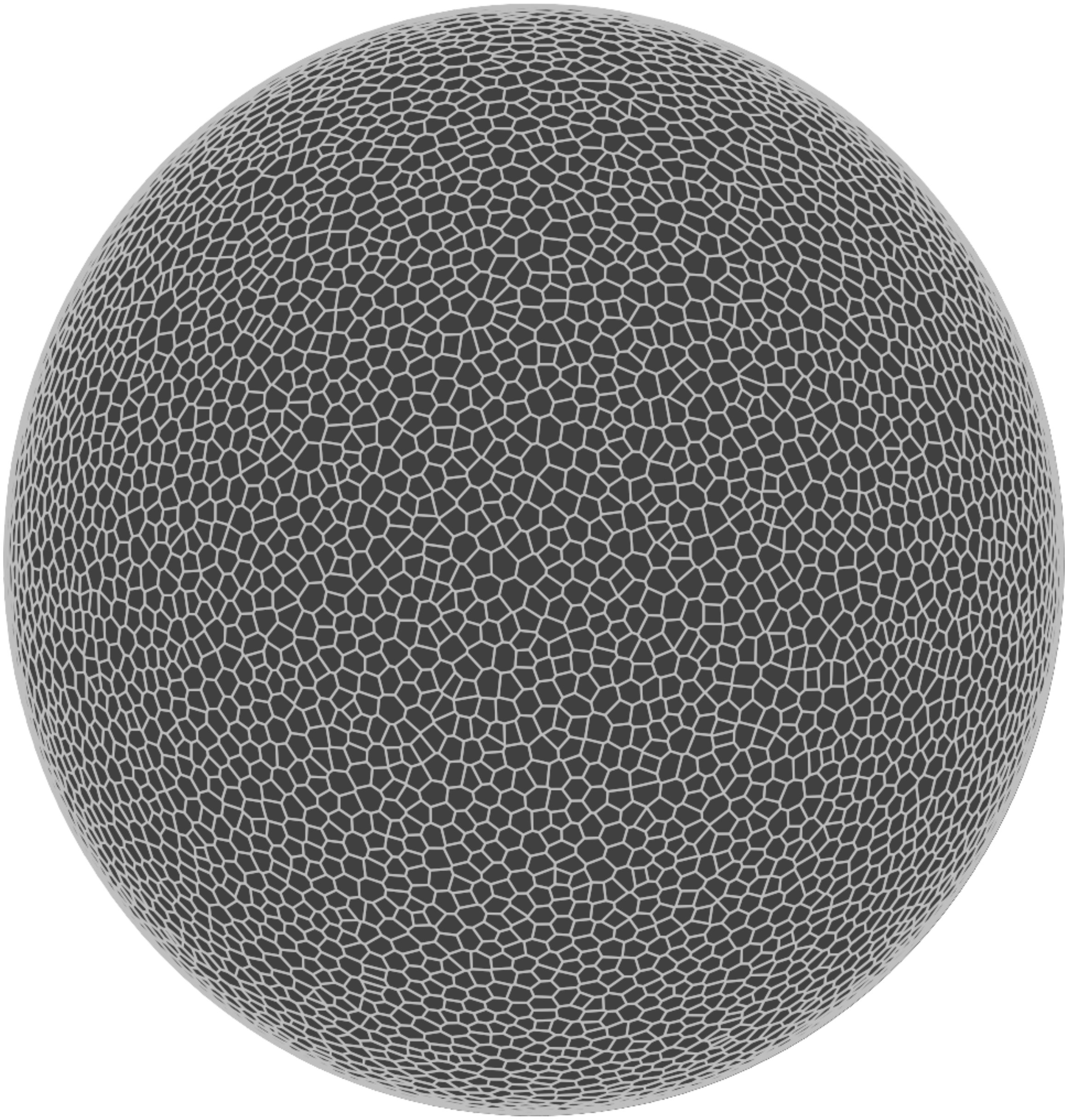

Figure 2.1: A 2D projection plot of the SCVT of N = 8000 cells on the surface of a sphere.

To reproduce the key aspects of this geometry, we use Spherical Centroidal Voronoi Tessellations (SCVT) to reproduce the geometry of the magnetic network. An SCVT on a sphere partitions the surface of the sphere into convex polygons, most of which are pentagons and hexagons as in figure 2.1. These are polygons represent very flat regions of the solar surface due to their relatively small size compared to the sphere. They are treated as 2-dimensional for all calculations, as are their Delaunay simplex duals. Reproducing the solar distribution of the area and shape of the SG convection cells is an important aspect of NFT. By choosing an accurate number for the number of SG on the solar surface, the SCVT algorithm reproduces the distribution and geometry of the SGs network pattern, to the precision of a classical polygon with straight boundaries.

The dual to the SCVT, the Spherical Delaunay Tessellations (SDT) is a useful geometric object for this simulation and is also generated. To find the Spherical Centroidal Voronoi Tesselation (SCVT), the Spherical Delaunay Tesselation (SDT) of N points confined to a spherical surface is calculated [Caroli et al., 2009]. An SDT divides the spherical surface into triangular facets where the vertices are the supplied generator points, as in figure 2.2. The SDT is used to find the SCVT with generator points normalized to the radius of the spherical surface. Because the SDT is a roughly spherical polyhedron of triangular facets, it has a dual polyhedron. A dual polyhedron has the vertices and the edges between pairs of vertices corresponding to the faces and the edges between pairs of faces of its dual. The dual polyhedron of the SDT is the SCVT. See figure 2.3 for an example of the relationship between SCVT ans SDT.

The centroid of each SCVT cell is calculated by finding the centroid of the vertices enclosing the cell. The entire SCVT is recomputed with the centroids as the generator points. This process is known as Lloyd's algorithm or Voronoi relaxation [Qiang et al., 2006]. This SCVT relaxation is iterated until the tesselation has the desired statistical distribution of properties. Figure 2.4 shows a typical distribution of cell areas and circularities. Circularity is a measure of the roundness of an object. A circle and any regular polygon has a circularity of 1. A perfectly relaxed SCVT

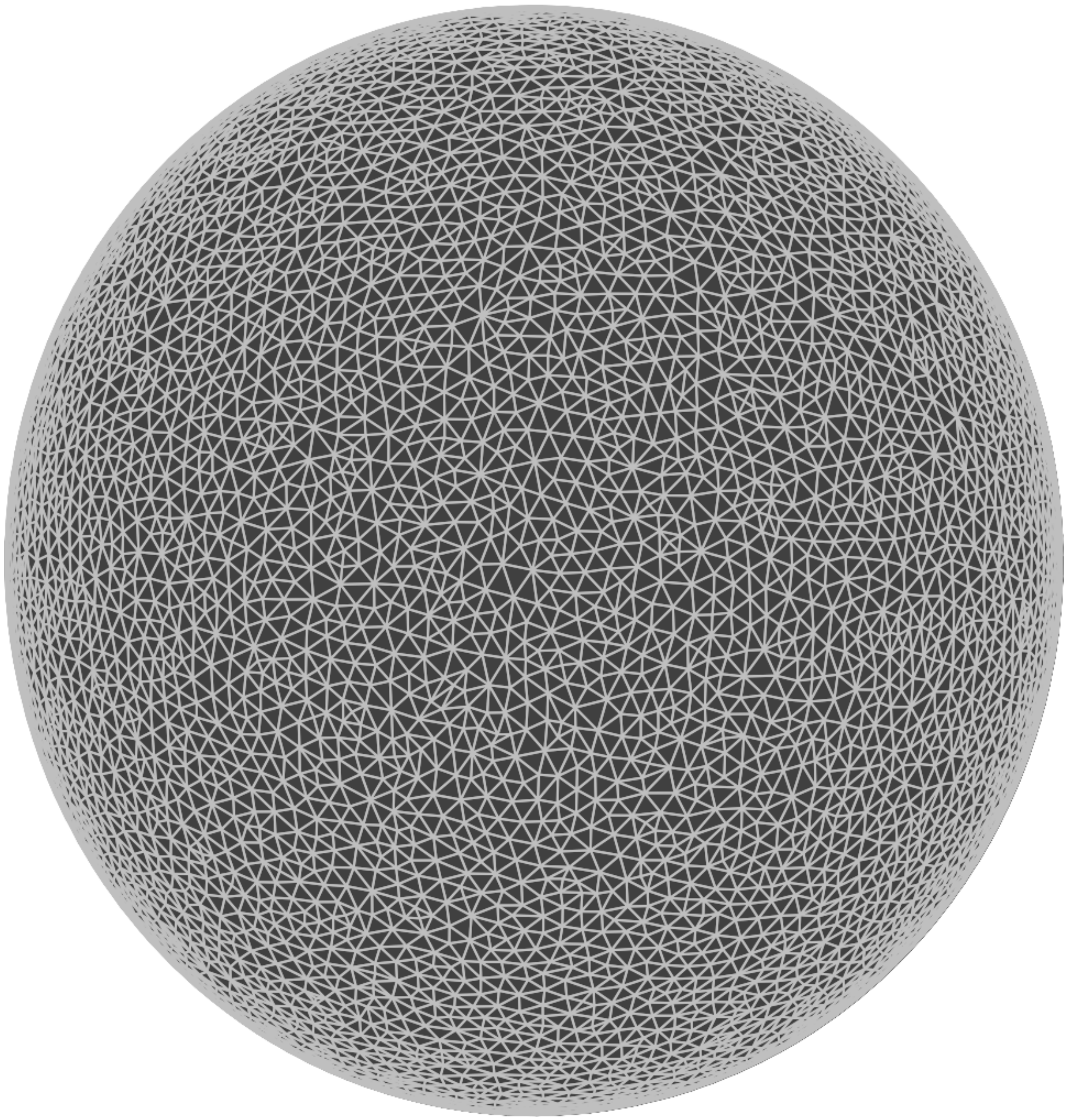

Figure 2.2: A representative depiction of the spherical centroidal Delaunay tesselation.

is a method of partitioning the surface of a sphere into SCVT cells of equal areas. Compare with figure 7 from Hagenaar et al. to see the observed area distribution [Hagenaar et al., 1997].

When calculating the advection of flux between timesteps, the displacement

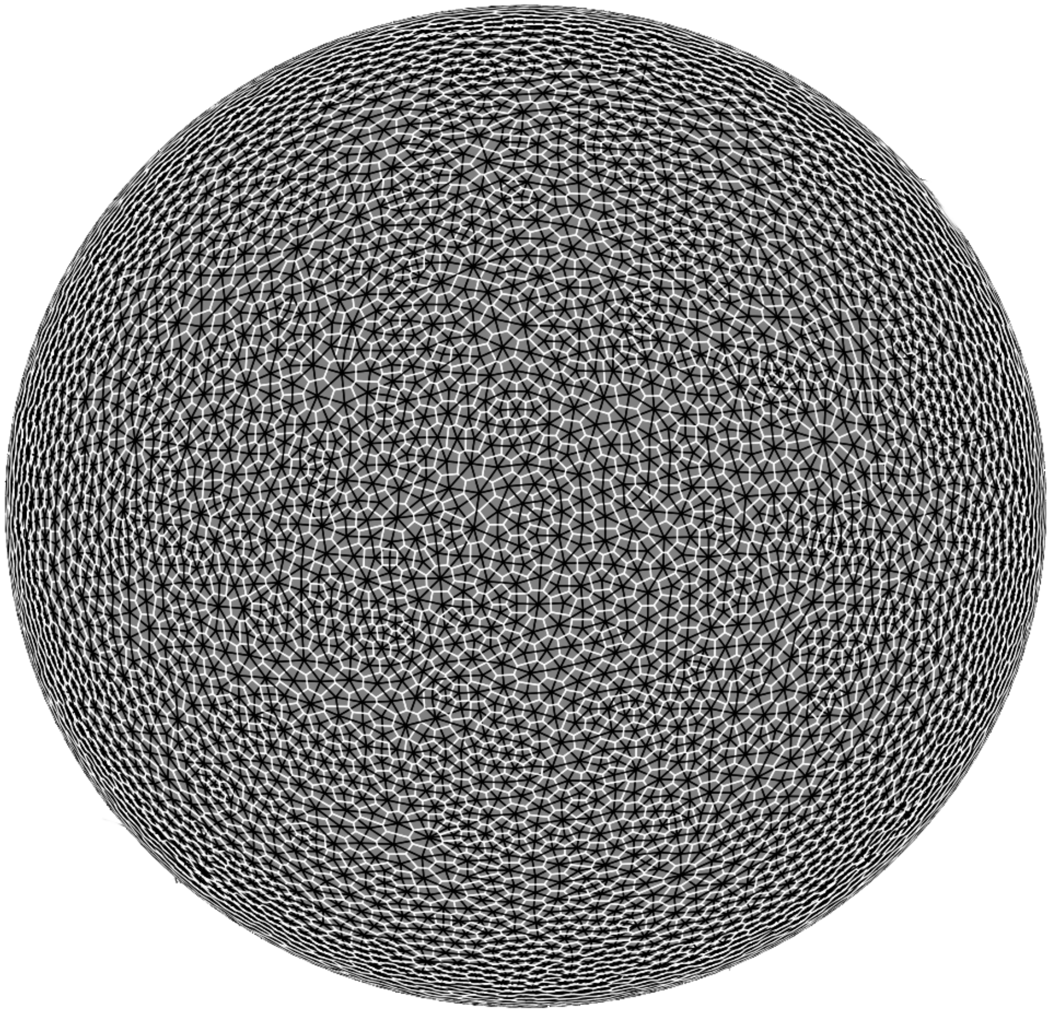

Figure 2.3: A plot showing the SDT / SCVT duality.

is calculated without numerically integrating a trajectory due to a velocity field. Because the displacements are occurring due to advection on the surface of a convecting domain, the displacements are assigned according to the configuration of the network cells. Flux is transported by displacing it to the nearest 2 vertices within the new network cell. The ability to calculate these displacements efficiently is one of the benefits of the SCVT framework.

Every timestep, a new random spatial configuration of the SCVT network

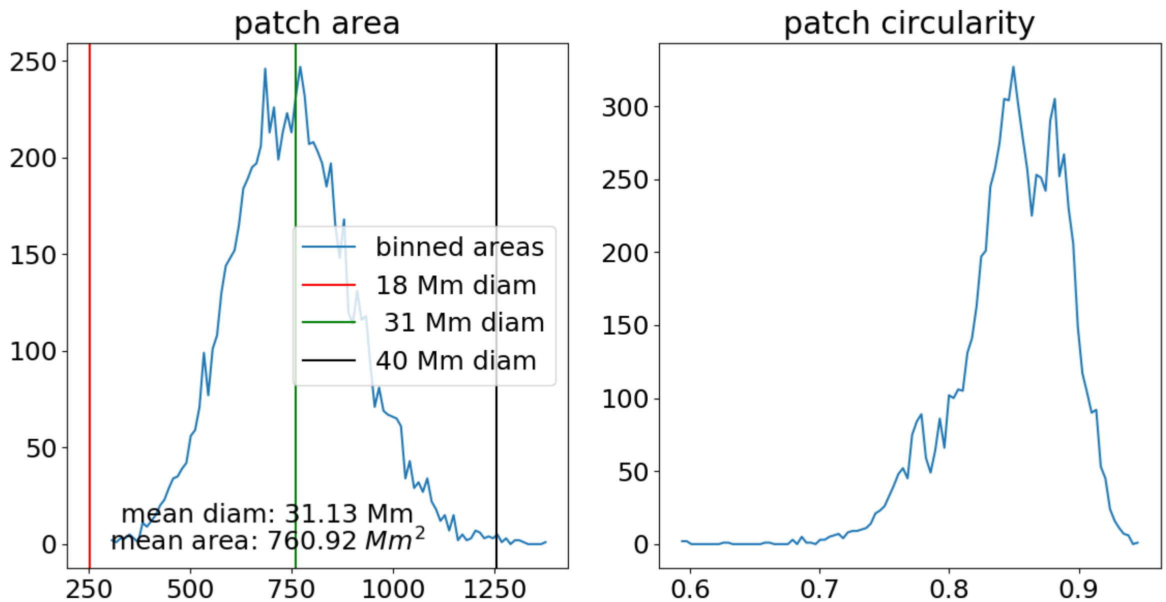

Figure 2.4: A plot of the SCVT area and circularity number distributions.

is calculated. This condition of a memory free SG configuration is currently a computational convenience and could be relaxed in a future version of the NFT method. What we've described in this section is the concept of NFT. Other simulation specific aspects of simulating the solar magnetic flux distribution are described in the following section.

We refer the interested reader to the code written in the Python scripting language, to be published with this thesis. To compute the SCVT, we utilize the Spherical Voronoi Tessellation package included within the SciPy library [Jones et al., 2001]. We have used a modified version of the SciPy SVT object code to allow for a larger number of Voronoi cells than was possible with the default implementation.

Simulation

The current version of the NFT simulation proceeds in a linear manner, described by the following outline:

1. Initialize variables and arrays with solar values.
2. Partition the solar surface into an SCVT.
3. Place an approximately quiet sun flux distribution of flux at the network vertices.
4. Begin iterative timestep portion of the simulation. This is repeated until the specified time period has elapsed, usually 2 solar cycles or 22 years:
   (a) add Intra-Network (IN) flux to the network.
   (b) add AR/ER flux to the polar perimeter.
   (c) create the new SCVT network.
   (d) fragment network flux near divergent flow center to the new network configuration, Figure 2.7.
   (e) advect network flux to the new network configuration, Figure 2.8.
   (f) Apply DR and MF displacements to new network using a product of the velocity and timestep.
   (g) calculate and record simulation output.

The following subsections are numbered according to the simulation outline, above.

1. Initialization

In this section, we describe the physical parameters used in the NFT simulation solar magnetic flux application. All values are chosen to be as near observed solar values as possible. The parameters are chosen from observation where available, and otherwise from published theoretical results. For calculations, the polar angle we use has the form having value $\theta = 0$ at the north pole and $\theta = 180$ at the south pole.

We use the value of 696 Megameters as the solar radius and choose 155520 seconds ($\approx$ 1.8 days) as the timestep for this simulation. This period is the average lifetime of an SG as published by Rincon et al. [Rincon and Rieutord, 2018].

To compare our simulation with a strictly SFT method with empirical diffusivity, we look at the parameters used for optimization in Whitbread et al. [Whitbread et al., 2017]. They identify 5 parameters, that they optimize to reproduce magnetogram data. The empirical diffusivity that they use (η), is an emergent behavior of NFT with dependence upon the number of SG cells we choose and the timestep. The 2 parameters to describe the MF are identical in our methods, as we use the simple functional form Whitbread et al. They explore the use of a magnetic field decay time-constant (τ) in some of their models. This parameter is a convenience parameter used in a paper by Schrijver et al. to promote the polar field reversal [Schrijver et al., 2002]. Field decay in NFT is not implemented, and does not appear to be a necessary physical process over the timescale of one full 22 year solar cycle. Finally, we choose a fixed value for the peak polar field B_o of 4 Gauss. We choose this value as it is roughly the maximum amplitude of the mean polar field from HMI polar observations (see figures 1.5 and 1.6).

2. Network tessellation

The solar SG network is a direct result of the surface convection that occurs on the sun and so is an appropriate application of NFT. The solar magnetic network is formed by a spatial flux distribution very similar to a spherical Voronoi tessellation. Both granulation and SG convection cells have been shown to have a similar geometry to Voronoi tessellations [Schrijver et al., 1997].

We partition the solar surface into 8000 SCVT polygons to represent the SG geometry (see figure 2.1). This number gives us the desired distribution of SG spatial scales. The number of active SG cells on the sun at any one time is a fluctuating quantity. We set this value constant for computational simplicity.

3. Initial flux distribution

Estimates of the quantity of quiet-sun unsigned flux on the solar surface at any one time are $\approx 10^{24}$ Mx. We place this quantity of flux in the network with a normal distribution of zero mean fluxes. The standard deviation is chosen computationally to produce the correct quantity of total unsigned flux, 10^{24} Mx. This reduces the number of time-steps needed to achieve the steady state distribution.

4. Iteration

The following steps are repeated in a loop representing the fundamental timestep of the system. For the solar network, the timestep is the 1.8 day mean supergranule lifetime.

a. IN flux We assume that granulation produces a stationary normal distribution of flux in the IN. Local flux neutrality requires that this distribution have a mean of zero. The standard deviation of this distribution (σ_{IN}) is estimated using observations. Using data from the SUNRISE balloon born IMAX magnetograph, Smitha et al. published a histogram of the observed flux distribution [Smitha et al., 2017]. The flux distribution has an apparent 3σ value of $\approx 10^{17}$ Mx. Also, Jin et al. observe an apparent 3σ value of $\approx 5 \cdot 10^{17}$ with Hinode/SOT, which has a lower resolution and larger FOV [Jin et al., 2009]. We interpret this discrepancy between 3σ values as SUNRISE/IMAX better resolving the granular network. As such we choose the SUNRISE value for our 3σ. Thus, $\sigma_{IN} = 3.334 \cdot 10^{16}$ as the standard deviation of our instantaneous IN flux distribution. We then use this to calculate the IN contribution to network flux.

The simulation calculates the flux contribution to the network from the IN, without explicitly tracking IN flux. This is done so that the NFT simulation accounts for the flux contributed to the network by IN sources [de Wijn et al., 2009]. Each timestep a quantity of flux is chosen from a normal distribution and is added to each of the network vertices. The mean of the normal distribution is zero, and the standard deviation (σ_{SG}) is the product of σ_{IN} with the the square root of the number of granulation network vertices within the inflow region for each network element. We use the average granule area of $1.33 Mm^2$ to estimate the number of granule cells inside each inflow region. The number of granular vertices in a closed Voronoi tessellation is roughly 2 times the number of cells. To establish the value of granular vertex flux for a given area, we assume the IN flux resides in the granulation network vertices between granules [de Wijn et al., 2009]. As we know the statistics for granule area and geometry, we know the number of random variables to draw from our nearly normal distribution for IN flux [Schrijver et al., 1997].

In figure 2.5, the red shaded triangles are the inflow regions of the SG cells. These are the regions that contribute flux to the contained SG network vertex, the blue dot. A granular network is shown only for scale reference as IN flux is not explicitly tracked. SG convection is assumed to advect flux (red arrow) away from an SG center (green X) and into the corresponding nearest network elements (blue dot). Each of the $\approx 16,000$ SDT simplices represent the inflow regions for their respective network vertices.

b. AR/ER flux To achieve a solar magnetic cycle, we add flux at the polar boundary of $\pm 55°$ latitude and let the MF carry it poleward. $\pm 55°$ is chosen as it represents a consistent observed boundary for two phenomena. It is the boundary for the polar coronal holes furthest extent towards the equator. It is also the furthest

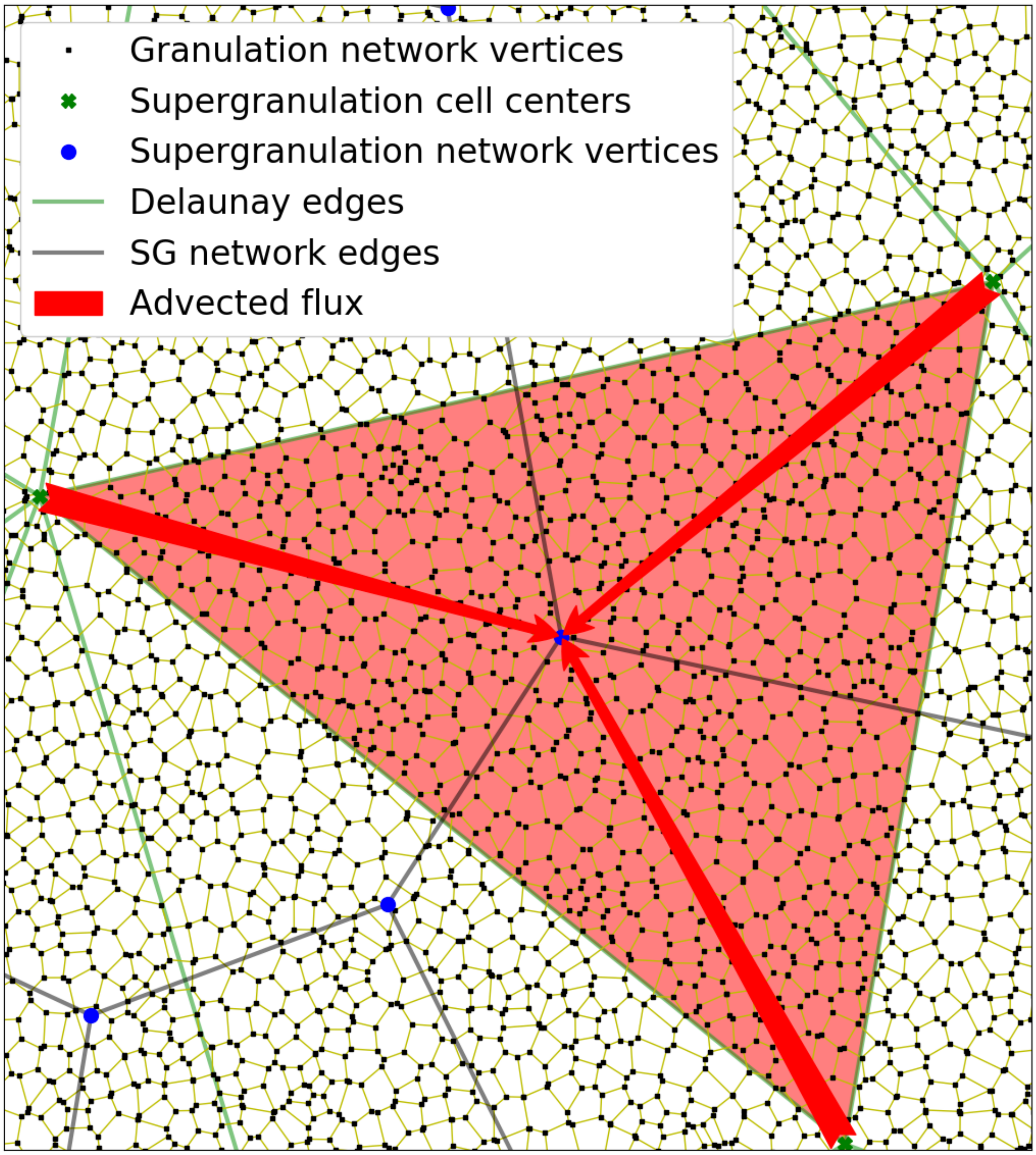

Figure 2.5: Overlay of SG Delaunay tessellation on SG and granulation networks to show the inflow region geometry relationships.

poleward latitude for flux emergence from the activity bands identified by McIntosh et. al. [McIntosh et al., 2014]. In this sense, 55° provides a consistent boundary for simulating polar phenomena.

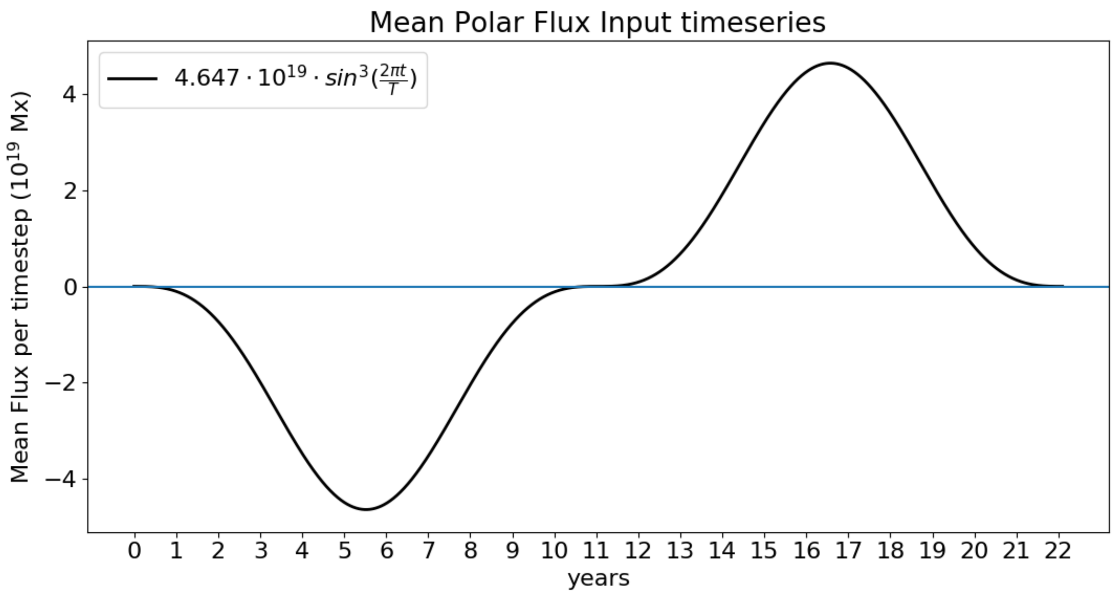

Figure 2.6: Normalized timeseries plot of mean polar flux rate added to polar boundary over two solar cycles.

We introduce the quantity of flux needed to change the polarity of the peak mean polar field within the polar area above 55°. We use an amplitude for the polar mean field (B_o) of 4 Gauss. The polar area above 55° has an area of $\approx 5.5e5 Mm^2$ and the mean polar field changes sign every 11 year half-cycle. The total quantity of flux that we place at the polar boundary is then calculated from these values for area and field. The quantity of flux needed to completely reverse the polar field from ∓ 4 to ± 4 Gauss over the entire polar area is $\approx \pm 4.4044 \cdot 10^{22}$ Mx. This flux is placed at the polar boundary with a cyclic waveform having a continuous quadratic curvature of amplitude $\approx 8.008 \cdot 10^{21} \frac{Mx}{year}$, as shown in figure 2.6. This waveform is chosen as a simplistic approximation to the contribution of flux from AR sources carried to the poles by the MF. This waveform has two key qualitative features to replicate the polar solar cycle. It is peaked, to reproduce the fast polar field reversal. It also has a flat, small amplitude portion to reproduce the hiatus during solar minimum.

We apply flux to the boundary in a variable number of flux elements. Using the value of $\pm 5e17$ Mx, the sign of the flux is determined by the phase of the solar cyclest mean value. The mean value of the polar flux injection rate tracks the timeseries value that we plot in figure 2.6. We use a Poisson arrival model as described in Pinsky et al., to choose the number of flux elements arriving per timestep [Pinsky and Karlin, 2011]. This involves using a Poisson distribution (equation 2.1) to choose the number of arriving flux elements per timestep (k) with a specified distribution mean (λ).

$$P(k) = \frac{e^{-}\lambda \cdot \lambda^{k}}{k!} \tag{2.1}$$

c. New SCVT network We assume that the SG network configuration is relatively static for the average SG lifetime, about 1.8 days. We thereby assume that the generative process for SG is not influenced by the current configuration of the surface flux and velocity fields. In other words, it doesn't depend upon the initial configuration of magnetic fields when choosing the new network geometry. The current method of producing a new SG network configuration is to randomly rotate the SCVT sphere. This provides a locally random network without the computational cost of generating a new SCVT network for each timestep.

d. SG fragmentation NFT assumes that initial network vertex flux located within a specified radius of a new SG center distributes its flux symmetrically into the surrounding network, figure 2.7. We thus impose the condition that flux within a specified fragmentation radius of the new SG center fragments in this way.

Langfellner et al. observed and reported a FWHM of 8 Mm for the mean SG network inflow region [Langfellner et al., 2015]. This region is the flux trapping structure at the network vertices. From this, we specify our fragmentation radius as half the FWHM value found by Langfellner et al., 4 Mm. These vertex downflows

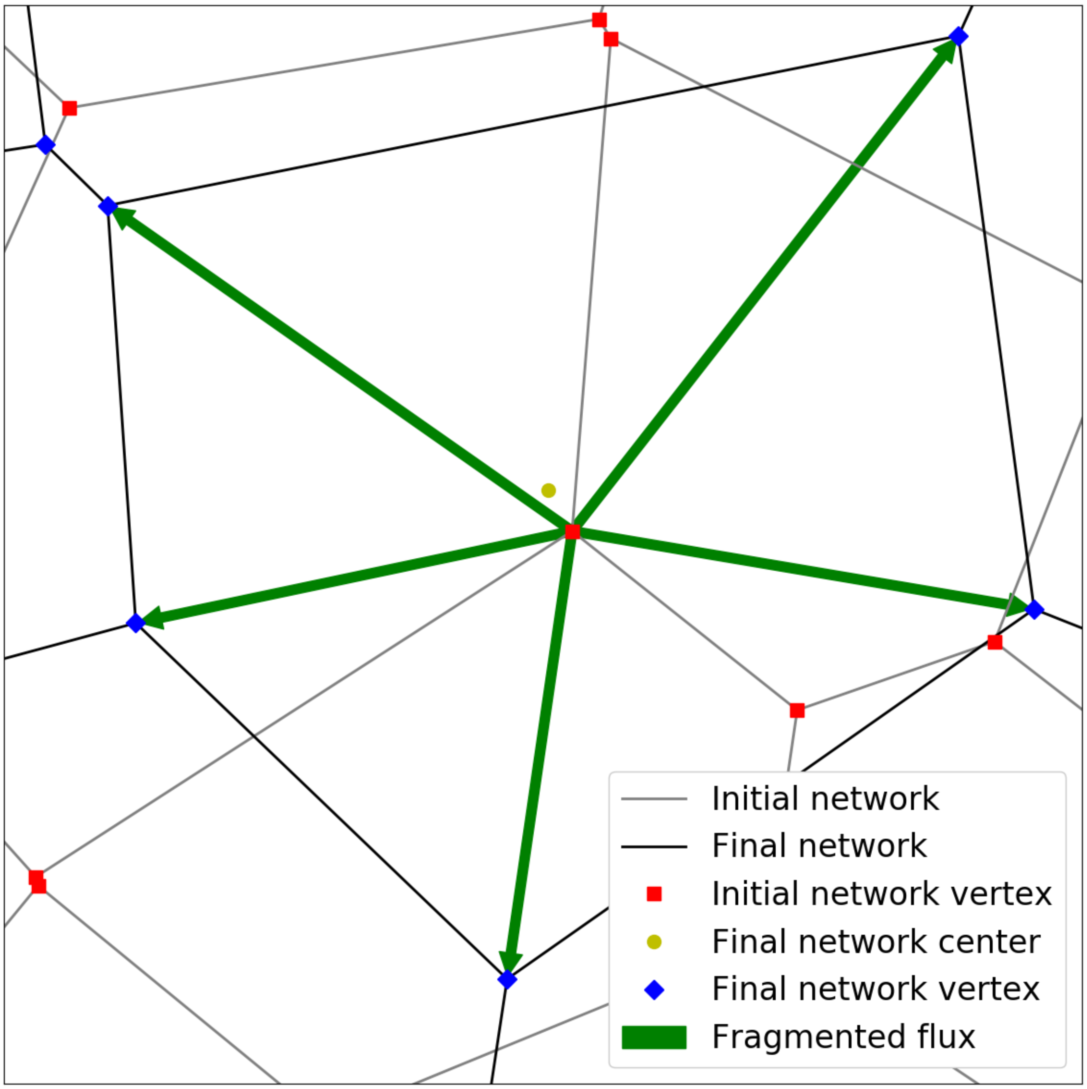

Figure 2.7: Example of magnetic network flux fragmenting in the case of proximity to SG center. The green arrows show the displacements of the initial flux for that timestep.

are areas of concentrated radial vorticity. The radial fields are also enhanced in these locations due to the similarity of the vorticity and B-field equations in turbulent MHD (see equations 1.2 and 1.3). If the new center of divergence is within this radius, the flux is considered to have fragmented radially into all surrounding network elements.

The frequency of a fragmentation event will depend entirely upon parameters which are simulation specific.

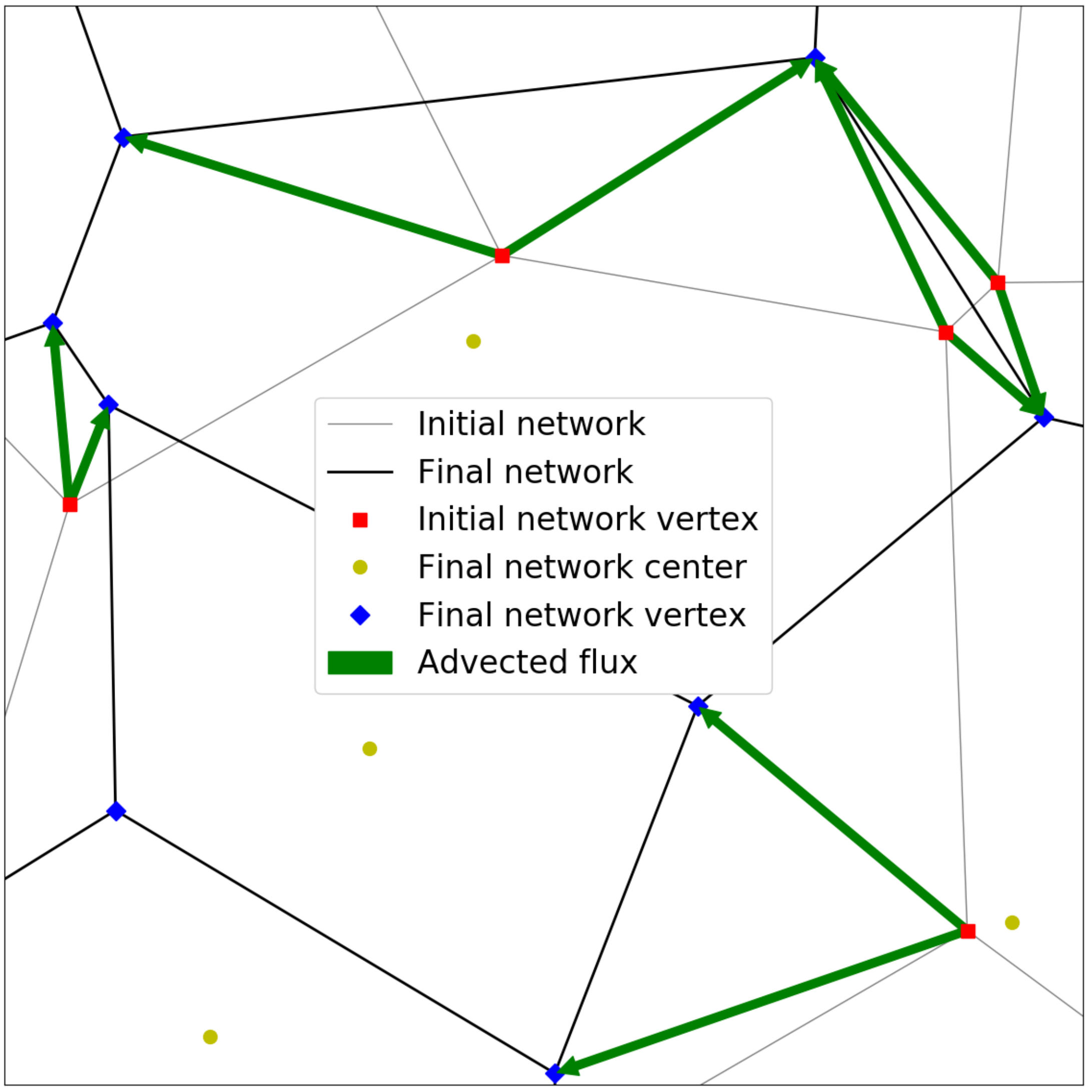

Figure 2.8: Example displacements of magnetic network flux between two timesteps. The green arrows show the displacements of the initial flux for that timestep.

e. SG advection SG advection transports the initial magnetic flux elements into the nearest two network vertices, as in figure 2.8. This flux division is weighted by the inverse distance between flux and the new network vertices, with the nearer new vertex receiving more of the flux. This bifurcation simulates the process of the spreading of the flux from the initial vertex as it enters the new network. As the flux flows outward to the network, it expands and shears with the diverging velocity flow of the SG.

For each flux element, we calculate the two nearest network vertices in the new SCVT network. The flux is then split weighted by the inverse distance to the final vertices. For example, if the initial flux element is Φ and the distances to the two nearest vertices are r1 and r2, then the two resultant flux elements would have $\Phi_{r1} = \Phi \cdot \frac{r1^{-1}}{r1^{-1}+r2^{-1}}$ and $\Phi_{r2} = \Phi \cdot \frac{r2^{-1}}{r1^{-1}+r2^{-1}}$ respectively. These terms simplify to $\Phi_{r1} = \Phi \cdot \frac{r2}{r1+r2}$ and $\Phi_{r2} = \Phi \cdot \frac{r1}{r1+r2}$. This flux is then added to the two nearest vertices, as in figure 2.8.

<u>f. DR and MF advection</u> We define the meridional flow as in equation 2.2 and 2.3. It is the same form used in Whitbread et al. with an exponent of n = 4 [Whitbread et al., 2017]. The MF function of the polar angle f_{MF} is computationally normalized by its maximum value and scaled to the desired maximum velocity, v_0. The MF profile for n = 4 has a maximum poleward value at $\approx 25°$ of $v_0 = 15\frac{m}{s}$. This is the peak value in the dynamic range seen by Hathaway et al. in their observation of MF velocities [Hathaway and Upton, 2014]. The analytical MF velocity function is plotted in figure 3.1 (right side, blue curve).

For DR we use the latitude dependent profile for magnetic features published in [Snodgrass and Ulrich, 1990]. We also remove the constant component of the rotation and use only the latitude variable components. For this simulation, the variation in toroidal velocity is the important information. The latitude independent, constant rotation of the sun plays no part in this simulation. We assume the complete

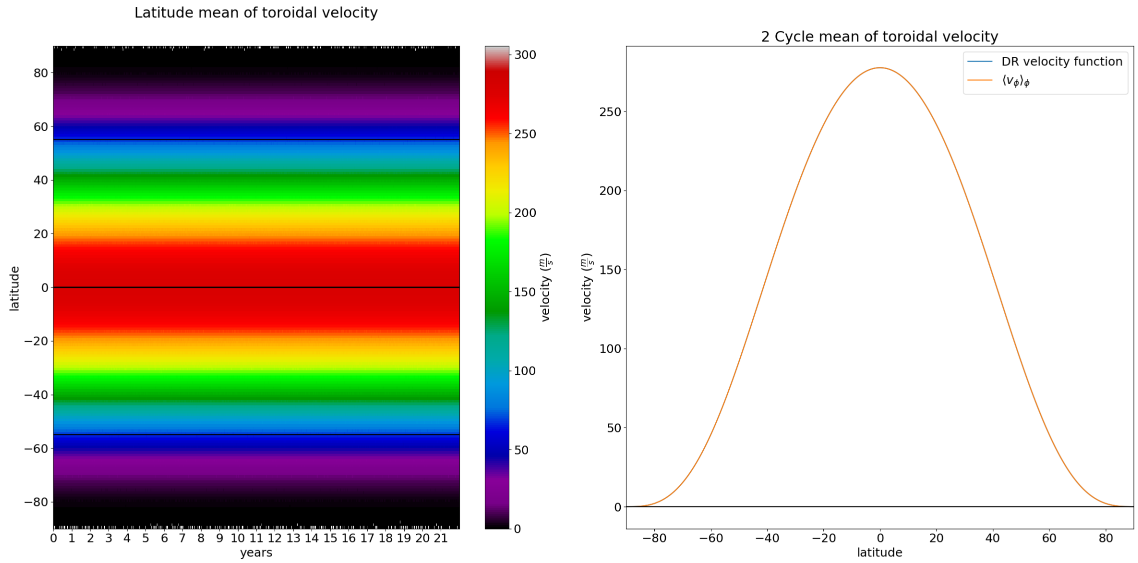

Figure 2.9: (left) Latitude mean of toroidal velocity. (right) Time average of toroidal velocities as a function of latitude compared to applied DR velocity function

lack of time dependence in the DR and MF. Time dependent variations in the DR and MF are associated with AR and ER flux in the activity belts [Zhao et al., 2014]. Because we explore the magnetism of the polar regions in this simulation, these time dependent effects are ignored.

$$f_{MF}(\theta) = \sin^4\theta \cos\theta \tag{2.2}$$

$$v(\theta) = -v_0 \cdot \frac{f_{MF}(\theta)}{max[f_{MF}(\theta)]} \tag{2.3}$$

g. simulation output The calculation and display of the desired simulation output is the motivation for this concept. As discussed in the following section, these outputs will be application specific. For our purposes, we will track:

1. macroscopic SG diffusion.

2. apparent MF

3. Mean Polar Field

4. Polar Flux Distribution

5. Simulated Magnetogram (Spatial flux Map)

RESULTS AND DISCUSSION

Applications

To test the validity of the NFT approach, we can identify some key observations of the simulation as applications. They are described in the following subsections with the results for each to be presented in the next section of the thesis. We will herein show an example of NFT output. NFT will be used to show the result of a single simulation run for 2 solar cycles using fixed parameters. The results are discussed below and can be summarized as qualitatively reproducing solar behavior at the poles.

SG diffusion

As an application of our NFT method, we can calculate the global mean of effective SG diffusivity for network vertex flux, every timestep using equation 1.1. For the length scale, we calculate the distance between the final and initial network locations. We take the global average of this displacement length to calculate the final value. Because the flux is constantly splitting during advection, we also use the flux weighted average of the fragments displacements. The time scale is the timestep for the simulation which is the average SG lifetime, 1.8 days. This diffusivity parameter should not be taken as representing a fundamental physical process for the sun. It exists as a simplification to represent the transport effect of velocity fields from surface convection.

Leighton's estimated value of $\approx 803\frac{km^2}{s}$ for SG diffusivity is larger than currently observed values. Schrijver et al used 5 day long datasets of Big Bear Solar Observatory magnetograms to observe a D of 250 $\frac{km^2}{s}$ [Schrijver and Martin, 1990]. Hagenaar et al. did a similar study of two sequences of MDI magnetograms and observed a range of 200 - 250 $\frac{km^2}{s}$ for SG timescales. Wang et al compares values of 500 and 250 $\frac{km^2}{s}$ in two different scenarios for a global scale SFT simulation [Wang, 2017]. Giannattasio observed effective diffusivity for IN flux concentrations and reported a range of 100 - 400 $\frac{km^2}{s}$ [Giannattasio et al., 2014].

Given that NFT explicitly tracks the advection of network flux concentrations due to SG, these values are applicable to this work. Also, because NFT only operates on the scale of the SG network, an NFT simulation will only account for the SG component of advective diffusivity. Some effective diffusion should occur from IN flux contributing flux to the SG network. Also, the explicit diffusivity due to the granulation velocity fields is not currently in the NFT simulation.

Meridional Flow

We can compare an observed MF as an output of the NFT simulation. Because we know the exact analytical function for the meridional flow applied to the simulation, any discrepancies between the two become apparent and can lead to a better understanding on how to measure MF. We can also compare the resulting mean field distribution to observed distributions to compare latitude dependent models of the MF.

Mean Polar Field

Calculation of the mean magnetic field for a region is another trivially obtained output of the NFT simulation method. By summing the flux in the desired area, and dividing by the magnitude of the area, we arrive at the field averaged over the entire area. One attractive option is the mean polar field, a commonly observed global manifestation of the solar cycle [Wang, 2017].

If the average field for an area is desired, we can take the area mean of all flux values in the specified area. This can also be done on a per pixel basis as the associated Delaunay tessellation simplex or the area enclosing the flux, is directly available. Finally, if an average field for the network itself is desired, an area for the network could be assigned to the flux used to calculate the areal average.

This measure has a strong dependence on the MF profile and speed. As has been stated in the applicable literature, "The polar cap flux densities are a function of the maximum latitude up to which the meridional flow effectively transports the flux." [Schrijver and Title, 2001] Because of this strong dependence, the MF profile can be inferred via a forward method simulation to find parameters that define the MF function. This is essentially what is done in Whitbread et al. using an SFT model [Whitbread et al., 2017]. The relative simplicity of an NFT model makes it an attractive option for such simulations.

Polar Flux Distribution

The polar flux distribution is one of the least complicated aspects of solar magnetism to track using NFT. Discrete network flux values are a fundamental variable within the NFT simulation. Binning and plotting a histogram are all that is needed to calculate and track. Because NFT doesn't incorporate the explicit distribution of the IN flux, it is necessary to add an IN flux distribution after the fact for comparison with the Shiota et al. results.

Spatial Flux Map

Perhaps the most important output of a simulation of solar surface flux is the spatial flux map of the spherical solar surface. The observational counterpart of this is a magnetogram. Because NFT flux is located only in the network, the resultant output will have the geometry of the NFT network. If we apply the colormap used by the HMI magnetogram, we will have a diagnostic tool for how closely the output map reproduces observation.

Supergranular Diffusion

Using the displacement of network vertex flux, we calculate the per timestep diffusivity constants. We use the flux weighted average of the 2 advective displacements per network vertex as the length scale for finding D from equation 1.1. Using these mean displacements, we calculate an effective D for each flux displacement and take the average over all displacements to establish the average over 2 solar cycles for D. The mean value of all the timestep averages of D for 2 solar cycles is 206 $\frac{km^2}{s}$. The observed range as referenced in the previous section of this thesis is 200 - 250 $\frac{km^2}{s}$ [Schrijver and Martin, 1990, Hagenaar et al., 1999]. Thus, there is strong agreement between the observed values and our simulated values for SG network scale diffusivity. Given that there is no simulation of a granular diffusion process occurring in NFT, an undervalued estimate is reasonable.

Meridional Flow

We measure the latitude mean of poloidal velocity. This is done by comparing the difference in polar angle before and after all advections have been applied. We then convert the units to meters per seconds. We find that the mean poloidal velocity matches the applied MF function with small fluctuations around the applied MF. Our analysis of apparent measured MF as an output of the NFT simulation compares favorably with the map of the MF from [Upton and Hathaway, 2014] and displayed in figure 1.3. Because the polar field has a strong dependence on the MF, the output of this simulation could be used to infer the actual latitude dependence of the MF by using a systematic scan of the parameter space.

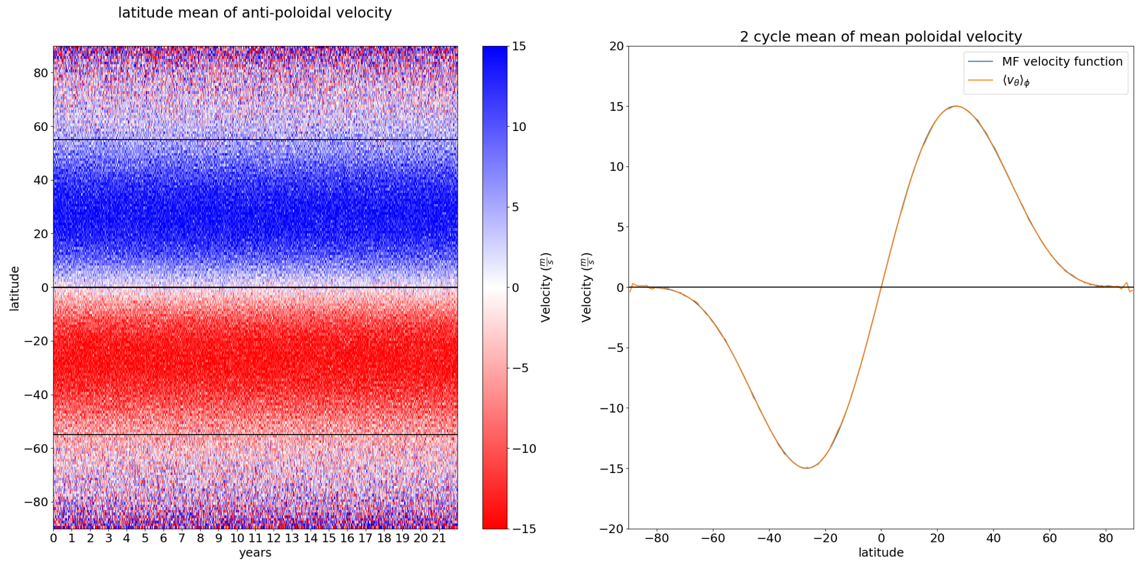

Figure 3.1: (left) Latitude mean of poloidal velocity measured by tracking the displacement of network vertices between timesteps.(right) Time average of poloidal velocities as a function of latitude compared to applied MF velocity function.

Mean Polar Field

We measure and analyze the behavior of the polar field in the NFT simulation. A comparison can now be made with the HMI results of Sun et al. [Sun et al., 2015] which we plotted in figures 1.5 and 1.6. This timeseries is generated by dividing the total flux in the poles by the area of the polar caps above ±55° latitude to produce the timeseries plots in figure 3.2.

NFT successfully reproduces the qualitative behavior of the polar mean field with simple assumptions. The behavior seen in both observation and simulation of the polar mean field timeseries is superficially a noisy sinusoidal signal with period of 22 years [Svalgaard et al., 1978, Sun et al., 2015, Wang, 2017].

The timeseries of the NFT mean polar field in figure 3.2, has this same distinctive behavior. It changes sign every 11 years based upon the contribution of flux arriving

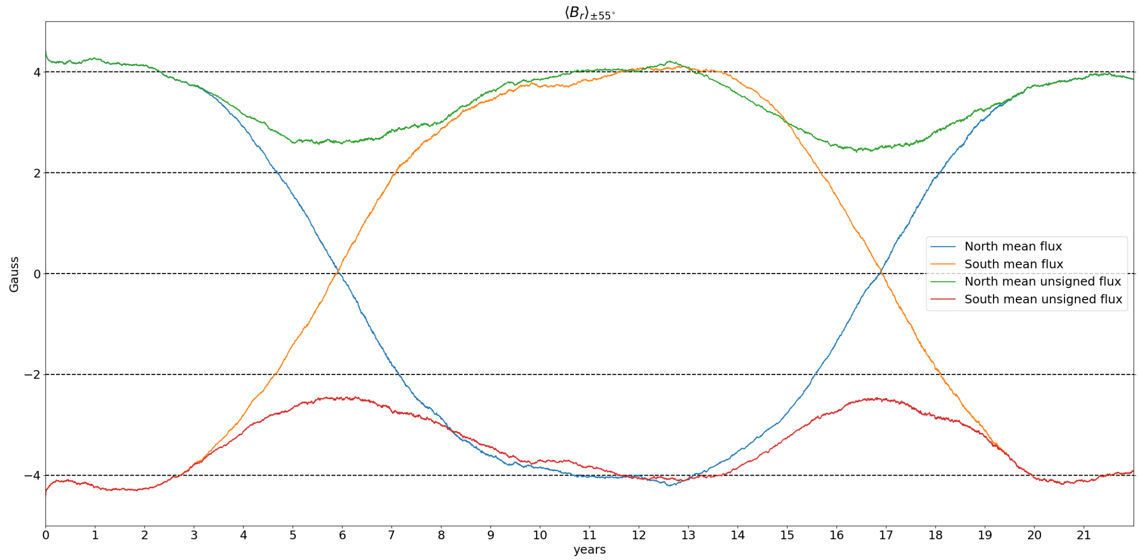

Figure 3.2: Timeseries plot of NFT simulated polar fields over 2 solar cycles.

from the $\pm 55°$ input latitude. Calculating the mean field of the poles acts as an integrating filter of the sum of this advected flux. The polar field waveform approaches a sinusoidal shape as it is dominated by the longest wavelength Fourier component of the input flux timeseries. The polar field inside the $\pm 55°$ polar boundary takes 4-5 years to reverse in both NFT and observations [Sun et al., 2015, Wang, 2017].

The observed waveform of new polar flux is not as smooth as our polar timeseries and can actually have large excursions due to the emergence of reverse polarized or "rogue" ARs [Nagy et al., 2019, Jiang et al., 2015]. The observed polar field is affected by the relative tilt of the Earth and Sun rendering a fraction of the poles unobservable. Regardless, the smoothing property of the poles integrating new flux leads to a similarly sinusoidal waveform.

We have also mapped the spatial distribution of the latitude binned average field, as in figure 3.3. This is a representation that is frequently used to demonstrate the output of SFT simulations, as well as the cycle variation of magnetograms [Jiang

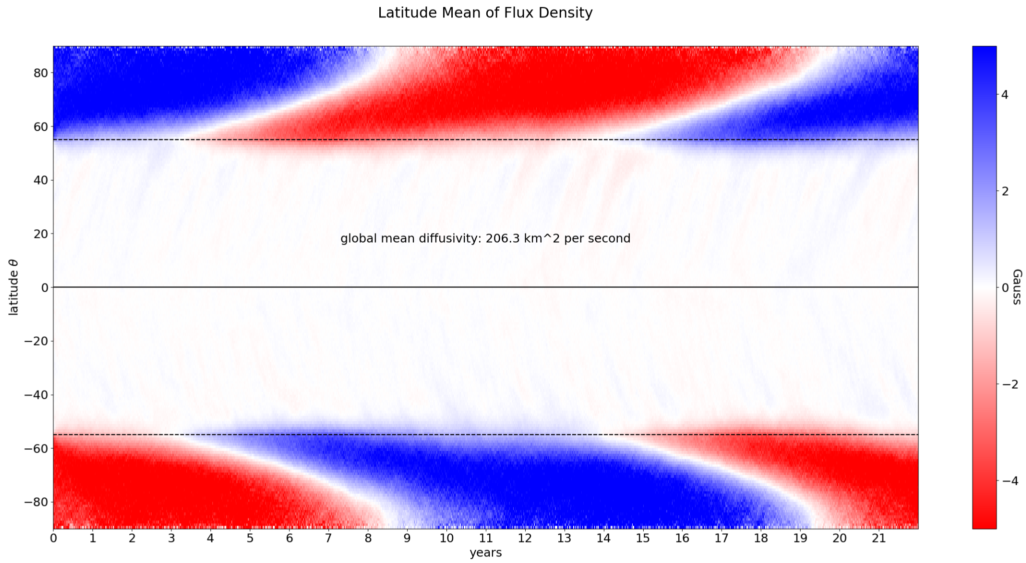

Figure 3.3: Time-latitude diagrams of the longitudinally averaged radial magnetic field at the solar surface over 2 solar cycles.

et al., 2015, Whitbread et al., 2017, Wang, 2017]. NFT successfully reproduces this distinctive pattern of the longitudinally averaged radial magnetic field inside the polar cap. The map in figure 3.3 demonstrates the cyclic polar field reversal.

Polar Flux Distribution

Qualitatively speaking, Shiota et al. [Shiota et al., 2012] finds that most magnetic flux in the polar regions, resides in large clusters of flux. This is true for both polarized and transitional phases of the solar polar cycle. See figure 1.8 in the introduction of this thesis.

To directly compare the Shiota et al. results with those from NFT, we must proceed mindfully of the differences in the underlying results. The Shiota results are sensitive to and include flux contributions from the Intra-Network (IN) magnetic flux distribution while NFT does not simulate the IN flux explicitly. Shiota also observes a smaller value for the polar mean field amplitudes than a simultaneous measurement

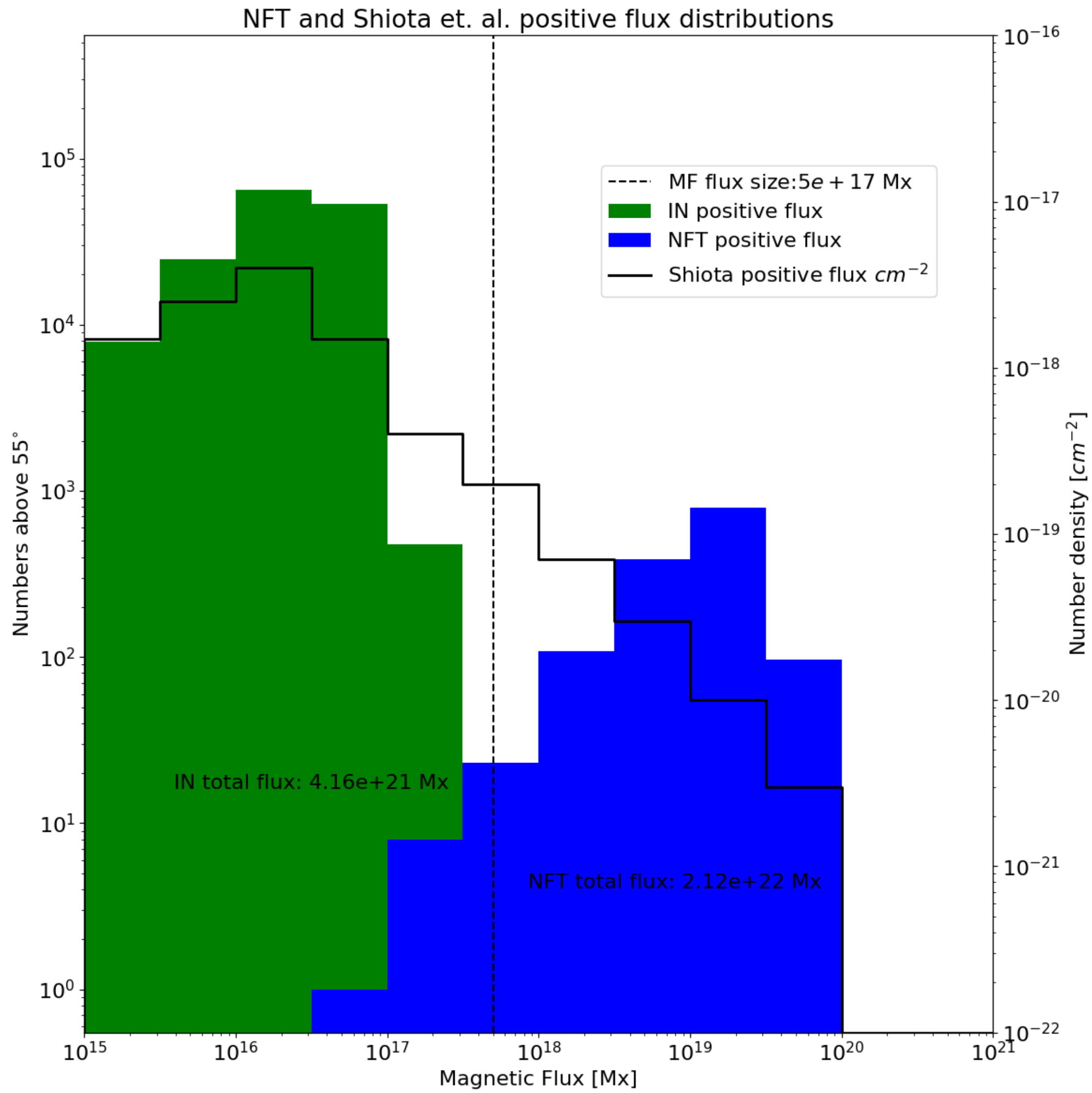

Figure 3.4: Comparison of NFT results with a representative positive polar flux distribution from figure 2b in [Shiota et al., 2012] or top center in figure 1.8, herein. Positive flux is the dominant polarity at this time.

made by the HMI polar field effort [Sun et al., 2015]. Shiota does report similar mean field values as WSO, but for different observed solar regions. WSO measures the immediate area of the poles whereas the Shiota observations are a snapshot of the center of the visible solar polar region (see figure 1 in [Shiota et al., 2012]). It

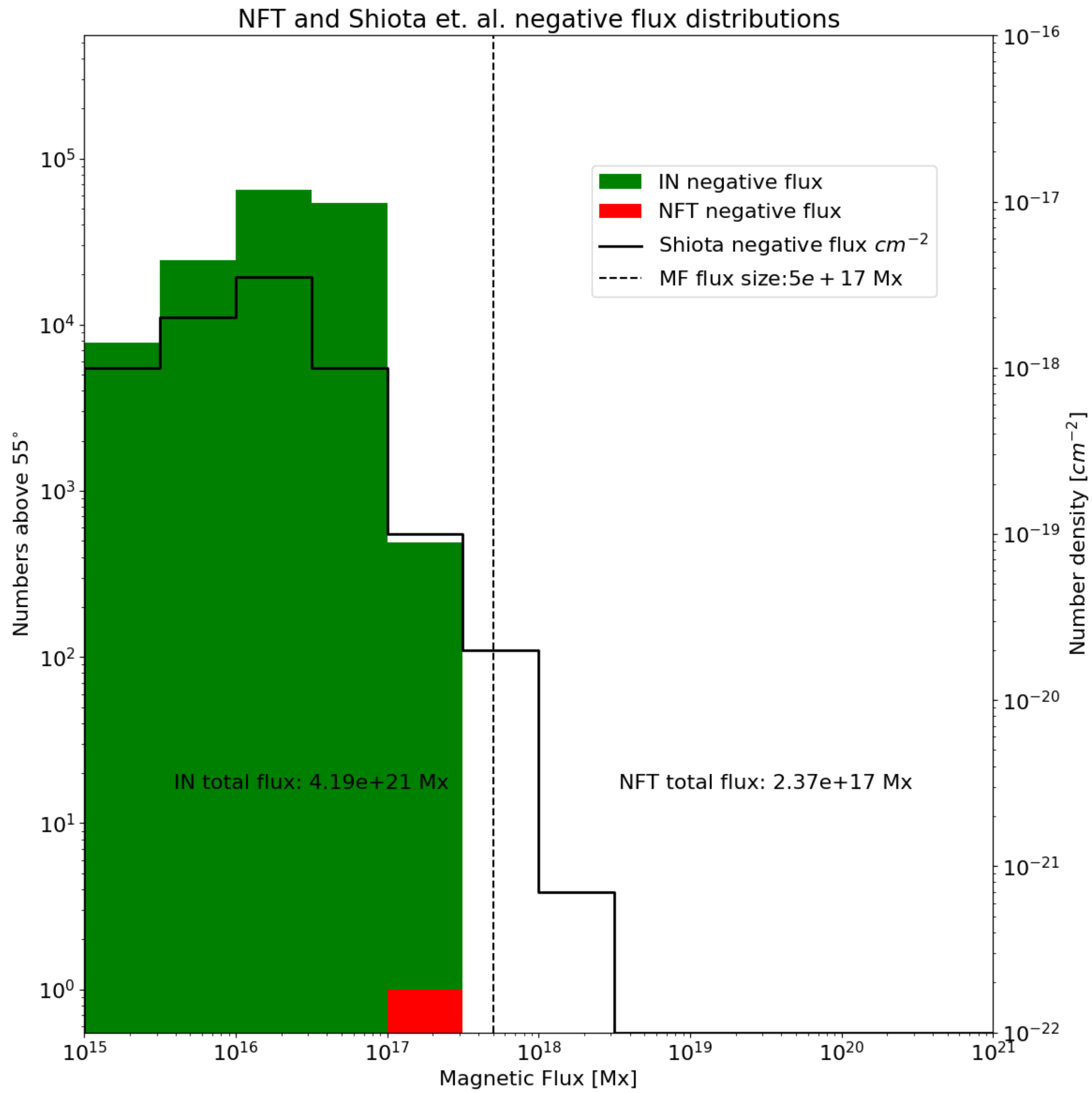

Figure 3.5: Comparison of NFT results with a representative negative polar flux distribution from figure 2b in [Shiota et al., 2012] or top center in figure 1.8, herein. Negative flux is the minority polarity at this time.

seems likely that the Shiota results undercount the total integrated flux, possibly due to the high obliquity of the solar surface near the poles and to unresolved small flux features.

We can assume that the IN has a stationary flux distribution, and then stack

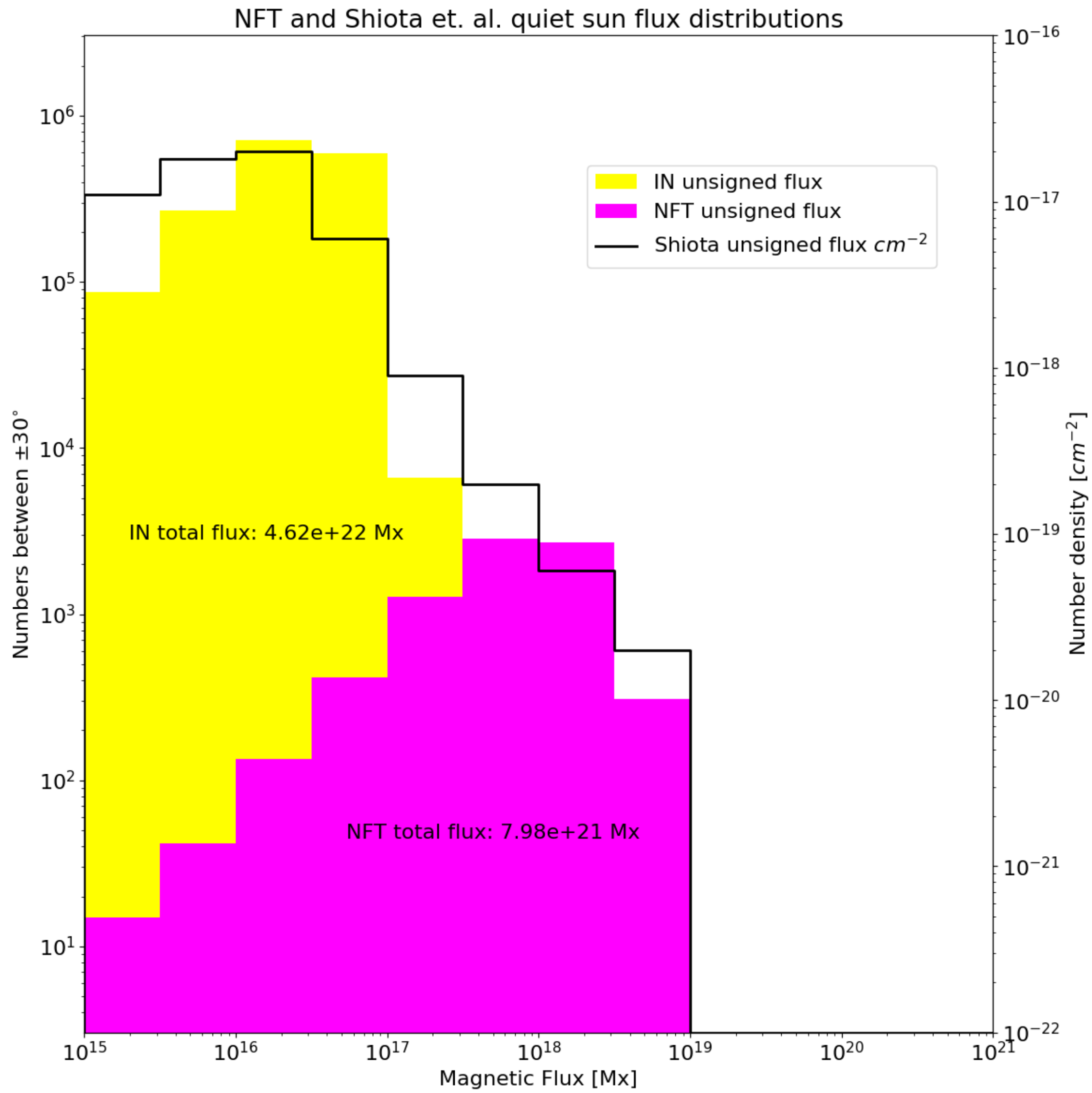

Figure 3.6: Comparison of NFT results with a representative quiet sun equatorial flux distribution from figure 2c in [Shiota et al., 2012] or top right in figure 1.8, herein. This figure shows unsigned flux as quiet sun flux neutrality results in an even, zero mean flux distribution.

the distribution on top of the NFT result. We choose a normal distribution with a standard deviation of $3.34 \cdot 10^{16}$, as we described in section 3. Doing so allows us to demonstrate the plausibility of the NFT flux distribution compared to the Shiota distribution. As we see in figure 3.4 the NFT flux distribution counts more elements than the Shiota results for the dominant polarity flux. Figure 3.5 shows an undercount by NFT of the minor polarity network elements. This effect is due to the limited spatial resolution of the NFT method. The actual solar spatial flux distribution is bumpy and non-uniform in the network due to granulation. A clustering method that can resolve the solar network, could create multiple smaller clusters from a single NFT element with significant flux. Because of this resolution issue, NFT accumulates more flux into single elements, than would be done by an observational clustering. Also worth mentioning here is the inability of NFT to form polar faculae. This is essentially when the network is overfull of a single polarity of flux and it spreads out into the IN granulation network. The statistics of the formation of polar faculae has been explored [Kaithakkal et al., 2013], and could be incorporated into a future version of NFT.

We present a comparison between an NFT quiet sun example, and the flux distribution for the Quiet Sun (QS) regime shown in Shiota's figure 2c as shown above in figure 3.6. Our QS distribution for NFT is taken from all latitudes below $\pm 30°$ where the simulation is in a perpetual QS regime. NFT here reproduces an extreme version of the QS regime. Typically, there are 2 activity belts present in each solar hemisphere, whereas NFT has none. This result is perhaps the most satisfying of the current version of the NFT simulation. It compares a low latitude observation of magnetic flux without the possibility of high obliquity observational issues to NFT results and finds a remarkable degree of agreement. The differences between the simulated distributions and the Shiota et al. observed distribution can be understood as the following. The IN and NFT distributions are not in equilibrium as they do not explicitly interact. The IN flux distribution is added and displayed only as a qualitative comparison. They are also spatially distinct as the IN and NFT flux occupies the two separate regions of the SG intra-network and the SG network, respectively. This explains the difference in simulated and observed distributions. Most observational results are agnostic about whether flux is in the IN or SG network and making the distinction takes careful analysis [Gošić et al., 2014]. A solution to this inconsistency would require a granulation scale NFT simulation.

Our results for the quantity of the flux contained in the NFT network are also too small. The total whole sun unsigned flux contained in the quiet sun network is estimated to be in the range of $\approx 10^{24}$ Mx [Gošić et al., 2016]. The NFT results suggest a value of $\approx 1.5 \cdot 10^{22}$, off by two orders of magnitude. The cause of this likely comes down to a resolution issue. NFT reports a sum of signed flux in each network vertex, in which there is typically cancellation of opposite polarity flux during the sum. The unsigned value is a sum of the absolute value of all flux in the network which is always a value greater than or equal to the net flux. The net sum of the signed flux is correct, but it is a distinct observable from the unsigned flux.

Spatial Flux Map

Lastly, we display the spatial map of solar magnetic flux as simulated by NFT. This is the raw data from which all other statistical results in this thesis are derived. We plot our maps centered at both north and south poles as these regions are the focus of the NFT applications for this thesis. We convert the map to magnetic field units by taking the quotient of flux and network area per vertex. We assume that the flux uniformly fills the entire vertex element, and that the network is 3 granule vertices in width. The HMI colormap is calibrated to show the difference between AR/ER field strengths, and the relatively weak SG network field strengths. See figure 3.7 for an example. There is a discontinuity in the colormap at ± 236 Gauss reflecting the difference in observed B-field regimes [HMI science-team, 2012].

Network flux is usually found in the larger clusters of flux forming incomplete

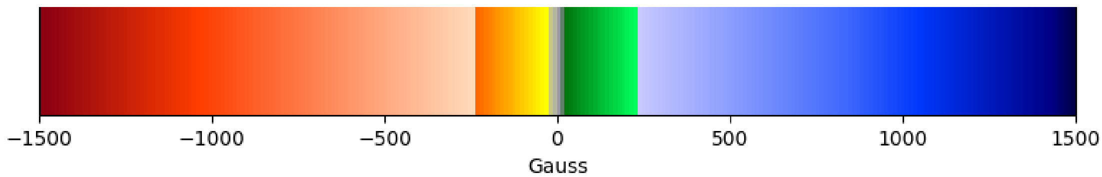

Figure 3.7: The HMI colormap used to colorize the field strength of magnetograms in Gauss.

rings. The relatively small IN flux patches are visible within the relatively large network rings. We have included an HMI magnetogram in figure 3.8 to display the true complexity of the solar magnetic network to compare to the relatively simple NFT.

These polar maps display the spatial distribution of polar flux during polar max, as in figure 3.9. The long term periodic variation in the polarity of flux is also apparent due to the AR/ER activity belt contributions of flux to the polar regions. The network field shows us where polar faculae would likely form, in the regions of the higher field strength. We also see that the NFT network fields remain in the range of network field strength as defined by the HMI colormap. It doesn't reach into the AR values of red and blue are where magnetic flux would overfill the network. This is useful as a diagnostic result as it reproduces the network field strength present in the poles.

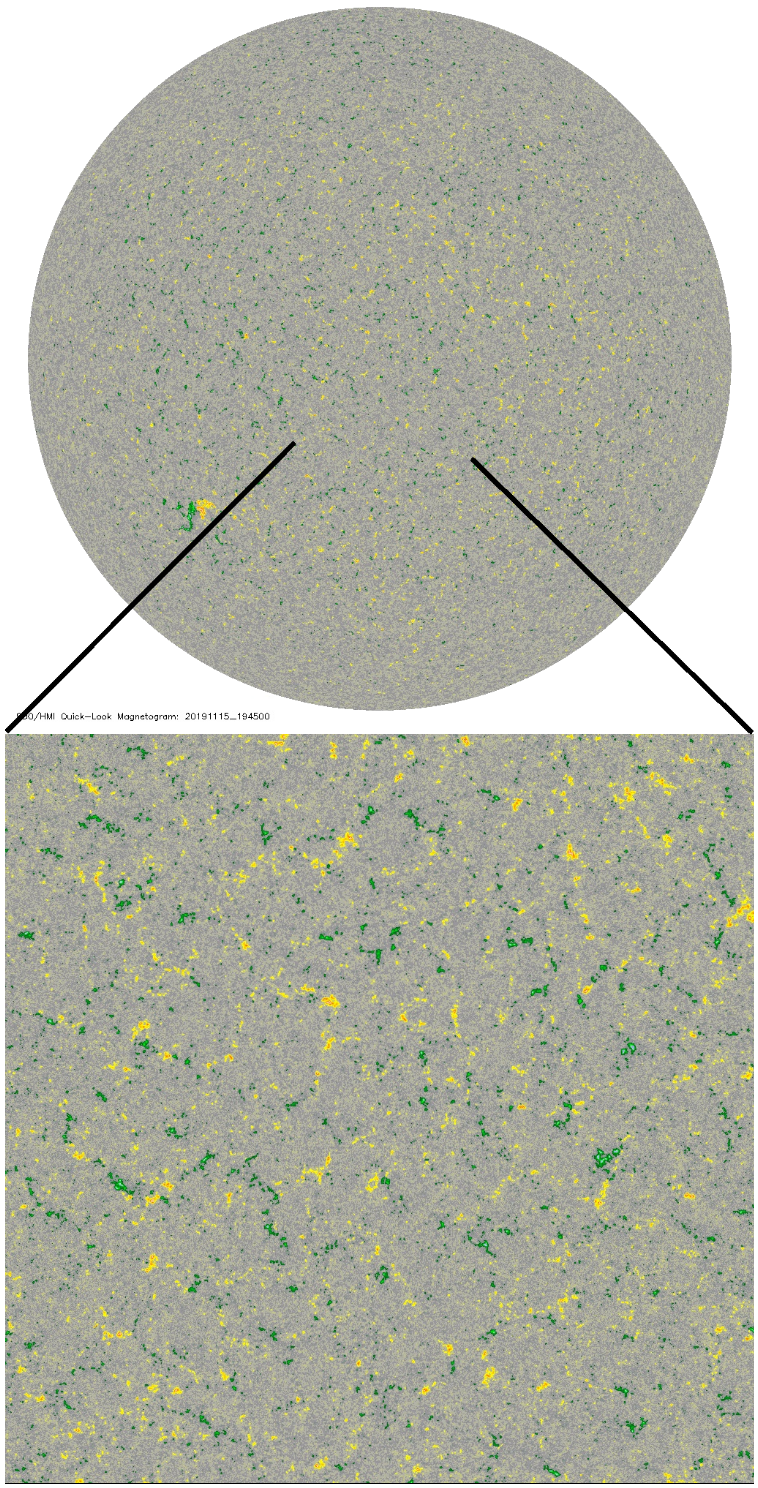

Figure 3.8: An HMI full disk magnetogram (top) with a zoom into the disk center(bottom).

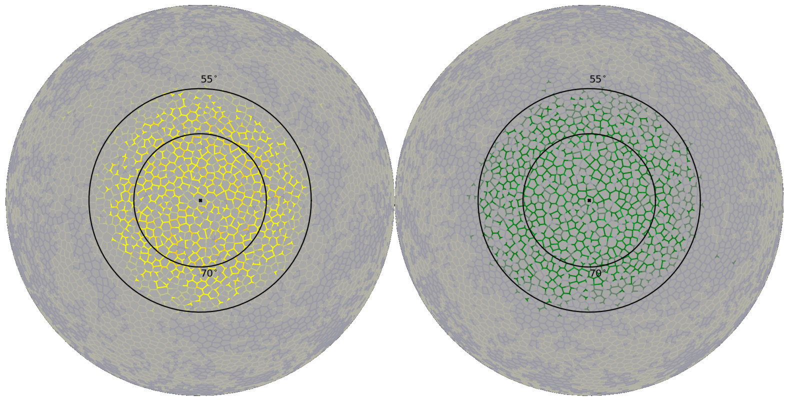

Figure 3.9: Two synthetic magnetograms from the NFT simulation of the solar poles. Magnetic field strength is color scaled with the HMI colormap. The North and South poles are on the top and bottom, respectively.

CONCLUSIONS

In this thesis, we have reviewed the relevant history of solar astronomy and physics, to provide context for the key concepts of NFT. We have described the conceptual and computational underpinnings of NFT. We then describe the results from an application of the NFT simulation to the suns polar magnetism. And finally, we discuss our conclusions from all of this effort.

By utilizing the network properties of the solar SG magnetic flux distribution and flow fields, we show it is possible to simulate solar polar magnetic behavior. We also show that it is possible to simulate the behavior, time evolution, and statistical properties of the quiet sun photospheric magnetic field to the spatial and time scales of the network. This is demonstrated by comparing several observable emergent properties of photospheric magnetism to those generated by our NFT simulation.

We compare the effective macroscopic diffusivity due to SG surface convection to observed values and find a high degree of agreement. We then look at the apparent meridional flow as measured by tracking magnetic flux, and find consistent flow behavior, as well as an apparent tracking anomaly near the poles. We have also implemented a method to simulate the magnetic solar cycle in the polar region of the sun. We use this to reproduce and map the polar mean field behavior, and find qualitative agreement with observed polar magnetograms. We also reproduce the polar magnetic flux distribution of discrete magnetic regions. This distribution we compare to an observed distribution and we again find qualitative agreement, with some differences. We describe, analyze, and attempt to explain the differences between the simulated and observed distributions.

NFT as described and utilized in this thesis is still in a conceptual, nascent form. Improvements in the computational efficiency and in the qualitative assumptions made in the simulation are still well within reach of a modest programming effort. Because the granulation convection network should behave in the same manner, there is nothing fundamentally preventing NFT from being adapted to the granulation scale, thereby increasing both time and spatial resolution of the simulation. It would however take a considerably larger amount of computing resources as the number of convection cells to calculate would increase by about 3 orders of magnitude. Because of this, extending NFT down to the granulation scale require more computing resources and a reasonable modification to the NFT code.

NFT is based on a few core emergent properties of magnetic flux on the solar surface, but could be applied to other phenomena. While it is certainly possible to simulate these processes in a 3D domain, the NFT simulation concept currently resides on the 2D surface of a 3D sphere. In the famous astronomy documentary Cosmos, Carl Sagan said "If you wish to make an apple pie from scratch, you must first invent the universe." To paraphrase Sagan, Because we wish to create a solar magnetic network we must first invent a network to hold our magnetic flux.

The magnetic field of the solar surface flux is the surface manifestation of a fundamentally 3 dimensional process. A scalar magnetogram is the radial projection of the solar magnetic field with the photosphere and not a fundamental structure. It is the nearly 2D cross section of a 3D field structure. It is important to keep this in mind when performing any 2D simulation of solar surface flux transport whether it's SFT, AFT or, NFT. NFT cannot make predictions about internal processes of the sun. It could in some future form be a component of a 3D spherical simulation of solar processes.

Also, there is considerable interest in the activity cycles of other stars. If an active star has near-surface convection like granulation and SG on the sun, then it will also accumulate fluctuating networks of magnetic flux. While these networks won't be directly observable in the near future, the effect of magnetic regions on their emission spectra are currently available. As such, a conceivable future application of NFT could be to represent a stellar network in a forward model to fit an observed spectral profile of an active or magnetic star.

From the favorable comparison of NFT results with the published literature demonstrated in this thesis, we can conclude that NFT is effective at modeling surface flux transport for the sun. NFT is a modeling technique which operates above a specific range of well defined spatial and temporal scales. In this case the scales are the length scale of the SG network and the lifetime of SG convection cells. Provided that the spatial and temporal resolution that one desires from a simulation is lower than the defined scales of the NFT simulation, the results are consistent with observed magnetic flux distributions on the solar photosphere.

REFERENCES CITED

[Babcock, 1959] Babcock, H. D. (1959). The Sun's Polar Magnetic Field. *ApJ*, 130:364.

[Babcock, 1953] Babcock, H. W. (1953). The Solar Magnetograph. *ApJ*, 118:387.

[Balogh and Thompson, 2009] Balogh, A. and Thompson, M. J. (2009). Introduction to Solar Magnetism: The Early Years. *Space Science Reviews*, 144:1–14.

[Basu, 2016] Basu, S. (2016). Global seismology of the sun. *Living Reviews in Solar Physics*, 13(1):2.

[Biskamp, 2003] Biskamp, D. (2003). *Magnetohydrodynamic Turbulence*. Cambridge University Press.

[Blanco Rodríguez et al., 2007] Blanco Rodríguez, J., Okunev, O. V., Puschmann, K. G., Kneer, F., and Sánchez-Andrade Nuño, B. (2007). On the properties of faculae at the poles of the Sun. *A&A*, 474(1):251–259.

[Borrero et al., 2017] Borrero, J. M., Jafarzadeh, S., Schüssler, M., and Solanki, S. K. (2017). Solar Magnetoconvection and Small-Scale Dynamo. Recent Developments in Observation and Simulation. *Space Science Reviews*, 210:275–316.

[Caroli et al., 2009] Caroli, M., Machado Manhães De Castro, P., Loriot, S., Rouiller, O., Teillaud, M., and Wormser, C. (2009). Robust and Efficient Delaunay triangulations of points on or close to a sphere. Research Report RR-7004, INRIA.

[de Wijn et al., 2009] de Wijn, A. G., Stenflo, J. O., Solanki, S. K., and Tsuneta, S. (2009). Small-Scale Solar Magnetic Fields. *Space Science Reviews*, 144(1-4):275–315.

[Eddy, 1976] Eddy, J. A. (1976). The Maunder Minimum. *Science*, 192(4245):1189–1202.

[Giannattasio et al., 2019] Giannattasio, F., Consolini, G., Berrilli, F., and Del Moro, D. (2019). The Complex Nature of Magnetic Element Transport in the Quiet Sun: The Lévy-walk Character. *ApJ*, 878(1):33.

[Giannattasio et al., 2014] Giannattasio, F., Stangalini, M., Berrilli, F., Del Moro, D., and Bellot Rubio, L. (2014). Diffusion of Magnetic Elements in a Supergranular Cell. *ApJ*, 788(2):137.

[Giles et al., 1997] Giles, P. M., Duvall, T. L., Scherrer, P. H., and Bogart, R. S. (1997). A subsurface flow of material from the Sun's equator to its poles. *Nature*, 390(6655):52–54.

[Gockenbach, 2006] Gockenbach, M. S. (2006). *Understanding And Implementing the Finite Element Method*. Society for Industrial and Applied Mathematics, Philadelphia, PA, USA.

[Gorobets et al., 2017] Gorobets, A. Y., Berdyugina, S. V., Riethmüller, T. L., Blanco Rodríguez, J., Solanki, S. K., Barthol, P., Gandorfer, A., Gizon, L., Hirzberger, J., van Noort, M., Del Toro Iniesta, J. C., Orozco Suárez, D., Schmidt, W., Martínez Pillet, V., and Knölker, M. (2017). The Maximum Entropy Limit of Small-scale Magnetic Field Fluctuations in the Quiet Sun. *ApJS*, 233(1):5.

[Gošić et al., 2016] Gošić, M., Bellot Rubio, L. R., del Toro Iniesta, J. C., Orozco Suárez, D., and Katsukawa, Y. (2016). The Solar Internetwork. II. Flux Appearance and Disappearance Rates. *ApJ*, 820:35.

[Gošić et al., 2014] Gošić, M., Bellot Rubio, L. R., Orozco Suárez, D., Katsukawa, Y., and del Toro Iniesta, J. C. (2014). The Solar Internetwork. I. Contribution to the Network Magnetic Flux. *ApJ*, 797(1):49.

[Hagenaar et al., 1997] Hagenaar, H. J., Schrijver, C. J., and Title, A. M. (1997). The Distribution of Cell Sizes of the Solar Chromospheric Network. *ApJ*, 481(2):988–995.

[Hagenaar et al., 1999] Hagenaar, H. J., Schrijver, C. J., Title, A. M., and Shine, R. A. (1999). Dispersal of Magnetic Flux in the Quiet Solar Photosphere. *ApJ*, 511(2):932–944.

[Hale, 1908] Hale, G. E. (1908). On the Probable Existence of a Magnetic Field in Sun-Spots. *ApJ*, 28:315.

[Harvey, 1993] Harvey, K. L. (1993). *Magnetic Bipoles on the Sun*. PhD thesis, , Univ. Utrecht, (1993).

[Harvey et al., 1999] Harvey, K. L., Jones, H. P., Schrijver, C. J., and Penn, M. J. (1999). Does Magnetic Flux Submerge at Flux Cancelation Sites? *Solar Physics*, 190:35–44.

[Hathaway and Upton, 2014] Hathaway, D. H. and Upton, L. (2014). The solar meridional circulation and sunspot cycle variability. *Journal of Geophysical Research: Space Physics*, 119(5):3316–3324.

[Herschel, 1801] Herschel, W. (1801). Observations Tending to Investigate the Nature of the Sun, in Order to Find the Causes or Symptoms of Its Variable Emission of Light and Heat; With Remarks on the Use That May Possibly Be Drawn from Solar Observations. *Philosophical Transactions of the Royal Society of London Series I*, 91:265–318.

[HMI science-team, 2012] HMI science-team, J. (2012). Hmi magnetogram colorscale.

[Iida et al., 2010] Iida, Y., Yokoyama, T., and Ichimoto, K. (2010). Vector Magnetic Fields and Doppler Velocity Structures Around a Cancellation Site in the Quiet Sun. *ApJ*, 713(1):325–329.

[Jiang et al., 2015] Jiang, J., Cameron, R. H., and Schüssler, M. (2015). The Cause of the Weak Solar Cycle 24. *ApJL*, 808(1):L28.

[Jin et al., 2009] Jin, C., Wang, J., and Zhao, M. (2009). Vector Magnetic Fields of Solar Granulation. *ApJ*, 690(1):279–287.

[Jones et al., 2001] Jones, E., Oliphant, T., Peterson, P., et al. (2001). SciPy: Open source scientific tools for Python.

[Kaithakkal et al., 2013] Kaithakkal, A. J., Suematsu, Y., Kubo, M., Shiota, D., and Tsuneta, S. (2013). The Association of Polar Faculae with Polar Magnetic Patches Examined with Hinode Observations. *ApJ*, 776:122.

[Komm et al., 1993] Komm, R. W., Howard, R. F., and Harvey, J. W. (1993). Meridional Flow of Small Photospheric Magnetic Features. *Solar Physics*, 147:207–223.

[Langfellner et al., 2015] Langfellner, J., Gizon, L., and Birch, A. C. (2015). Spatially resolved vertical vorticity in solar supergranulation using helioseismology and local correlation tracking. *A&A*, 581:A67.

[Leighton, 1964] Leighton, R. B. (1964). Transport of Magnetic Fields on the Sun. *ApJ*, 140:1547.

[Malherbe and Dalmasse, 2019] Malherbe, J. M. and Dalmasse, K. (2019). The New 2018 Version of the Meudon Spectroheliograph. *Solar Physics*, 294(5):52.

[Martinez Pillet et al., 2019] Martinez Pillet, V., Hill, F., Hammel, H., de Wijn, Dr., A. G., Gosain, S., Burkepile, J., Henney, C. J., McAteer, J. R. T., Bain, H. M., Manchester, IV, W. B., Lin, H., Roth, M., Ichimoto, K., and Suematsu, Y. (2019). Astro2020 Science White Paper: Synoptic Studies of the Sun as a Key to Understanding Stellar Astrospheres. *arXiv e-prints*.

[Maunder, 1904] Maunder, E. W. (1904). Note on the Distribution of Sun-spots in Heliographic Latitude, 1874-1902. *MNRAS*, 64:747–761.

[McIntosh et al., 2014] McIntosh, S. W., Wang, X., Leamon, R. J., Davey, A. R., Howe, R., Krista, L. D., Malanushenko, A. V., Markel, R. S., Cirtain, J. W., Gurman, J. B., Pesnell, W. D., and Thompson, M. J. (2014). Deciphering Solar Magnetic Activity. I. On the Relationship between the Sunspot Cycle and the Evolution of Small Magnetic Features. *ApJ*, 792:12.

[Muñoz-Jaramillo et al., 2013] Muñoz-Jaramillo, A., Dasi-Espuig, M., Balmaceda, L. A., and DeLuca, E. E. (2013). Solar Cycle Propagation, Memory, and Prediction: Insights from a Century of Magnetic Proxies. *ApJL*, 767(2):L25.

[Muñoz-Jaramillo et al., 2015] Muñoz-Jaramillo, A., Senkpeil, R. R., Windmueller, J. C., Amouzou, E. C., Longcope, D. W., Tlatov, A. G., Nagovitsyn, Y. A., Pevtsov, A. A., Chapman, G. A., and Cookson, A. M. (2015). Small-scale and Global Dynamos and the Area and Flux Distributions of Active Regions, Sunspot Groups, and Sunspots: A Multi-database Study. *ApJ*, 800(1):48.

[Nagy et al., 2019] Nagy, M., Lemerle, A., and Charbonneau, P. (2019). Impact of rogue active regions on hemispheric asymmetry. *Advances in Space Research*, 63(4):1425–1433.

[Needham, 1959] Needham, J. (1959). *Science and Civilisation in China: Volume 3, Mathematics and the Sciences of the Heavens and the Earth*.

[Nordlund et al., 2009] Nordlund, Å., Stein, R. F., and Asplund, M. (2009). Solar Surface Convection. *Living Reviews in Solar Physics*, 6:2.

[Parnell et al., 2009] Parnell, C. E., DeForest, C. E., Hagenaar, H. J., Johnston, B. A., Lamb, D. A., and Welsch, B. T. (2009). A Power-Law Distribution of Solar Magnetic Fields Over More Than Five Decades in Flux. *ApJ*, 698:75–82.

[Petrie, 2017] Petrie, G. (2017). High-Resolution Vector Magnetograms of the Sun's Poles from Hinode: Flux Distributions and Global Coronal Modeling. *Solar Physics*, 292:13.

[Petrie, 2015] Petrie, G. J. D. (2015). Solar magnetism in the polar regions. *Living Reviews in Solar Physics*, 12(5).

[Pinsky and Karlin, 2011] Pinsky, M. A. and Karlin, S. (2011). 5 - poisson processes. In Pinsky, M. A. and Karlin, S., editors, *An Introduction to Stochastic Modeling (Fourth Edition)*, pages 223 – 276. Academic Press, Boston, fourth edition edition.

[Priyal et al., 2014] Priyal, M., Banerjee, D., Karak, B. B., Muñoz-Jaramillo, A., Ravindra, B., Choudhuri, A. R., and Singh, J. (2014). Polar Network Index as a Magnetic Proxy for the Solar Cycle Studies. *ApJL*, 793:L4.

[Qiang et al., 2006] Qiang, D., Emelianenko, M., and Ju, L. (2006). Convergence of the lloyd algorithm for computing centroidal voronoi tessellations. *SIAM J. Numer. Anal*, pages 102–119.

[Rempel, 2014] Rempel, M. (2014). Numerical Simulations of Quiet Sun Magnetism: On the Contribution from a Small-scale Dynamo. *ApJ*, 789(2):132.

[Requerey et al., 2018] Requerey, I. S., Cobo, B. R., Gošić, M., and Bellot Rubio, L. R. (2018). Persistent magnetic vortex flow at a supergranular vertex. *A&A*, 610:A84.

[Rincon, 2019] Rincon, F. (2019). Dynamo theories. *Journal of Plasma Physics*, 85(4):205850401.

[Rincon and Rieutord, 2018] Rincon, F. and Rieutord, M. (2018). The sun's supergranulation. *Living Reviews in Solar Physics*, 15(1):6.

[Scherrer et al., 2012] Scherrer, P. H., Schou, J., Bush, R. I., Kosovichev, A. G., Bogart, R. S., Hoeksema, J. T., Liu, Y., Duvall, T. L., Zhao, J., Title, A. M., Schrijver, C. J., Tarbell, T. D., and Tomczyk, S. (2012). The Helioseismic and Magnetic Imager (HMI) Investigation for the Solar Dynamics Observatory (SDO). *Solar Physics*, 275(1-2):207–227.

[Schrijver et al., 2002] Schrijver, C. J., De Rosa, M. L., and Title, A. M. (2002). What Is Missing from Our Understanding of Long-Term Solar and Heliospheric Activity? *ApJ*, 577(2):1006–1012.

[Schrijver et al., 1997] Schrijver, C. J., Hagenaar, H. J., and Title, A. M. (1997). On the Patterns of the Solar Granulation and Supergranulation. *ApJ*, 475(1):328–337.

[Schrijver and Martin, 1990] Schrijver, C. J. and Martin, S. F. (1990). Properties of the Largescale and Smallscale Flow Patterns in and around AR:19824. *Solar Physics*, 129(1):95–112.

[Schrijver and Title, 2001] Schrijver, C. J. and Title, A. M. (2001). On the formation of polar spots in sun-like stars. *ApJ*, 551(2):1099.

[Schrijver and Zwaan, 2000] Schrijver, C. J. and Zwaan, C. (2000). *Solar and Stellar Magnetic Activity*. Cambridge Astrophysics. Cambridge University Press.

[Sheeley, 1964] Sheeley, Neil R., J. (1964). Polar Faculae during the Sunspot Cycle. *ApJ*, 140:731.

[Shiota et al., 2012] Shiota, D., Tsuneta, S., Shimojo, M., Sako, N., Orozco Suárez, D., and Ishikawa, R. (2012). Polar Field Reversal Observations with Hinode. *ApJ*, 753:157.

[Simon and Leighton, 1964] Simon, G. W. and Leighton, R. B. (1964). Velocity Fields in the Solar Atmosphere. III. Large-Scale Motions, the Chromospheric Network, and Magnetic Fields. *ApJ*, 140:1120.

[Smitha et al., 2017] Smitha, H. N., Anusha, L. S., Solanki, S. K., and Riethmüller, T. L. (2017). Estimation of the Magnetic Flux Emergence Rate in the Quiet Sun from Sunrise Data. *ApJS*, 229(1):17.

[Snodgrass and Ulrich, 1990] Snodgrass, H. B. and Ulrich, R. K. (1990). Rotation of Doppler Features in the Solar Photosphere. *ApJ*, 351:309.

[Solanki et al., 2010] Solanki, S. K., Barthol, P., Danilovic, S., Feller, A., Gandorfer, A., Hirzberger, J., Riethmüller, T. L., Schüssler, M., Bonet, J. A., and Martínez Pillet, V. (2010). SUNRISE: Instrument, Mission, Data, and First Results. *ApJL*, 723(2):L127–L133.

[Srivastava et al., 2018] Srivastava, A. K., McIntosh, S. W., Arge, N., Banerjee, D., Dikpati, M., Dwivedi, B. N., Guhathakurta, M., Karak, B., Leamon, R. J., Matthew, S. K., Munoz-Jaramillo, A., Nandy, D., Norton, A., Upton, L., Chatterjee, S., Mazumder, R., Rao, Y. K., and Yadav, R. (2018). The extended solar cycle: Muddying the waters of solar/stellar dynamo modeling or providing crucial observational constraints? *Frontiers in Astronomy and Space Sciences*, 5:38.

[Stenflo, 1982] Stenflo, J. O. (1982). The Hanle effect and the diagnostics of turbulent magnetic fields in the solar atmosphere. *Solar Physics*, 80:209–226.

[Stenflo, 2017] Stenflo, J. O. (2017). History of Solar Magnetic Fields Since George Ellery Hale. *Space Science Reviews*, 210(1-4):5–35.

[Sun et al., 2015] Sun, X., Hoeksema, J. T., Liu, Y., and Zhao, J. (2015). On Polar Magnetic Field Reversal and Surface Flux Transport During Solar Cycle 24. *ApJ*, 798:114.

[Svalgaard et al., 1978] Svalgaard, L., Duvall, T. L., J., and Scherrer, P. H. (1978). The strength of the Sun's polar fields. *Solar Physics*, 58(2):225–239.

[Tassoul, 2000] Tassoul, J.-L. (2000). *Stellar Rotation*. Cambridge Astrophysics. Cambridge University Press.

[Thomas and Weiss, 2008] Thomas, J. H. and Weiss, N. O. (2008). *Sunspots and Starspots*. Cambridge Astrophysics. Cambridge University Press.

[Tsuneta et al., 2008] Tsuneta, S., Ichimoto, K., Katsukawa, Y., Nagata, S., Otsubo, M., Shimizu, T., Suematsu, Y., Nakagiri, M., Noguchi, M., Tarbell, T., Title, A., Shine, R., Rosenberg, W., Hoffmann, C., Jurcevich, B., Kushner, G., Levay, M., Lites, B., Elmore, D., Matsushita, T., Kawaguchi, N., Saito, H., Mikami, I., Hill, L. D., and Owens, J. K. (2008). The solar optical telescope for the hinode mission: An overview. *Solar Physics*, 249(2):167–196.

[Upton and Hathaway, 2014] Upton, L. and Hathaway, D. H. (2014). Predicting the Sun's Polar Magnetic Fields with a Surface Flux Transport Model. *ApJ*, 780(1):5.

[Upton and Hathaway, 2018] Upton, L. A. and Hathaway, D. H. (2018). An Updated Solar Cycle 25 Prediction With AFT: The Modern Minimum. *GRL*, 45(16):8091–8095.

[van Ballegooijen et al., 1998] van Ballegooijen, A. A., Nisenson, P., Noyes, R. W., Löfdahl, M. G., Stein, R. F., Nordlund, Å., and Krishnakumar, V. (1998). Dynamics of Magnetic Flux Elements in the Solar Photosphere. *ApJ*, 509(1):435–447.

[Virkar and Clauset, 2014] Virkar, Y. and Clauset, A. (2014). Power-law distributions in binned empirical data. *Annals of Applied Statistics*, 8(1):89–119.

[Voronoi, 1908] Voronoi, G. (1908). Nouvelles applications des paramètres continus à la théorie des formes quadratiques. deuxième mémoire. recherches sur les parallélloèdres primitifs. *Journal für die reine und angewandte Mathematik*, 134:198–287.

[Wang, 2017] Wang, Y. M. (2017). Surface Flux Transport and the Evolution of the Sun's Polar Fields. *Space Science Reviews*, 210(1-4):351–365.

[Whitbread et al., 2017] Whitbread, T., Yeates, A. R., Muñoz-Jaramillo, A., and Petrie, G. J. D. (2017). Parameter optimization for surface flux transport models. *A&A*, 607:A76.

[Zhao et al., 2014] Zhao, J., Kosovichev, A. G., and Bogart, R. S. (2014). Solar Meridional Flow in the Shallow Interior during the Rising Phase of Cycle 24. *ApJL*, 789:L7.